Physics and Physical Oceanography Technical Report
2000-1

Circulation Through the Narrows of St. John's Harbour: Summer and Fall 1999

Brad deYoung, Douglas J. Schillinger, Len Zedel and **Jack Foley**

Department of Physics and Physical Oeanography
Memorial University of Newfoundland
St. John's, Newfoundland
A1B 3X7

Abstract

Current, temperature, fluorescence and surface elevation are presented from St. John's harbour for 24 July to 27 August and 12 October to 9 November 1999. Two Acoustic Doppler Current Profiler's (ADCPs) were deployed in July/August and one in October/November to measure the current velocities at the mouth of the harbour. Analysis of the current data shows that the flow over the sill is quite complex. The mean flow had a three-layer structure in July/August and a two-layer flow in October/November. The mean flow at the surface is out of the harbour during both periods. Transports computed from the current data were compared with results obtained using surface elevation observations from the harbour. There was reasonable agreement at tidal periods but very poor agreement at subtidal periods. Currents in the centre of the channel were not representative of the entire channel at subtidal frequencies. The amplitudes and phases of the five primary tidal constitutents show relatively little vertical structure except for the semi-diurnal band in July/August for which there is clear evidence of a baroclinic tide. An energetic band at about 0.5 cycles per day, coherent with the wind, was observed in July/August, but not in October/November.

Acknowledgements

We thank the St. John's Harbour Authority, in particular the Harbour Master, for permission to fool around in the middle of the channel - a rather busy spot. The Harbour Master also provided us with a detailed survey chart of the Narrows. We thank the divers from the Ocean Sciences Centre for their support and for working in a difficult area. We acknowledge the financial support of Environment Canada and the St. John's ACAP.

Table of Contents

List of Tables

List of Figures

Introduction

The city of St. John's is located on the Northeast coast of the Avalon Peninsula on the Island of Newfoundland, Canada. The harbour mouth opens to the east, has a large sill and a narrow entry to a shallow protected bay that has a somewhat deeper basin in the northeastern half of the harbour. The mean depth of the harbour is about 12-15 m, the sill depth is 13 m and the width of the harbour mouth is approximately 180 m. The deepest point of the harbour is about 33m. The channel leading to the sill, the Narrows, is approximately 800 m long and the harbour itself is about 1200m long. The harbour has a surface area of approximately 1.2 million square metres. The cross sectional area of the harbour mouth at the location of central channel mooring (depth 17m) is approximately 1600 square metres (Figure 1).

During the summer and fall of 1999 an upward-looking Acoustic Doppler Current Profiler (ADCP) was deployed in the centre of the harbour mouth at a depth of 17 m (see Figures 1 and 2). Our primary goal was to determine the circulation over the sill and the implications of the transport for the exchange of water into and out of the harbour. In July/August, an additional cross-channel-looking ADCP was deployed to one side of the harbour mouth at a depth of 5 m. Temperature sensors were located on the ADCP's and a fluorometer was deployed on the ADCP in the centre of the channel. Surface height data from the head of the harbour was obtained from the MEDS website (www.meds-sdmm.dfo-mpo.gc.ca/meds/Home_e.htm).

Mooring data is tabulated with statistics on the maximum, minimum, mean and variance in each velocity component in Tables 2 and 18 for July and October respectively. The velocity data are presented graphically: time series at selected depths, power spectral density of the hourly time series, profile plots, tidal ellipse plots and low-pass filtered sub-tidal plots. We also calculated the transport from the current data and the observed surface elevation. Tidal analysis was conducted on both the velocity and height data. The results are presented graphically, with summary statistics in tabular format.

Station Information

Near the sill, the channel entering St. John's Harbour is very narrow, measuring less than 200m across and we expected that a single mooring deployed in the centre of the channel at this location would provide reasonable measurements of the average along-channel velocity. Given the channel geometry, we believed that most of the flow would be directed along the axis of the channel. The additional ADCP deployed in August in side-looking mode was located on the southern side of the channel, pointed across the channel towards Chain Rock (see Figure 1). Both instruments provided useful data, which are presented and discussed in this report, although the side-looking ADCP only measured sensible currents on the far side of the channel.

Table 1: Mooring Locations

Deployment	Latitude	Longitude	Bin Width (m)	Depth (m)	Start	Stop	Sampling Interval (minutes)
Upward-Looking	47 33.97	52 41.29	1	17	24-Jul-99	27-Aug-99	20
Cross-Channel	47 33.97	54 34.98	8	17	24-Jul-99	27-Aug-99	20
Upward-Looking	47 33.97	54 41.29	1	18	12-Oct-99	09-Nov-99	20

Data Analysis

Data collected during the deployment and recovery of the instruments were first clipped from all the records. Isolated incidents of bad data points were eliminated using a simple linear interpolation scheme. For both the July and October data, all the bad data points were limited to periods near the times of deployment and recovery.

We determined the along-channel and cross-channel axes through a covariance analysis to locate the angle that minimized the variance along one component of a set of perpendicular axes. For both July and October, the result of this analysis was depth dependent, with October showing less variation in the angle with depth. The average orientation was 15^o clockwise rotation in July/August and 22^o clockwise rotation in October (see Figure 1). To minimise the cross channel velocity variation, the angles corresponding to each individual deployment were chosen, however, the difference in angle between deployments was only 7^o.

The surface was located by examining the backscatter intensity contours and identifying the depth bin with the most intense backscatter signal. Additional depth bins were discarded on the basis of shear in the velocity profile. For the upward looking ADCP, this resulted in the additional exclusion of two depth bins below the bin that recorded the maximum backscatter intensity in July and three depth bins in October. For the cross-channel velocity contour plots, the backscatter intensity contours are included because of the large intensity backscatter signal from intermediate bins. In the vertical, the depth resolution was roughly 1 m; for the side-looking instrument the horizontal resolution was roughly 8 m.

For tidal analysis, we applied the harmonic analysis routines of Foreman (1977), which require that the time series be in hourly intervals. To this end, data for the tidal analysis were first filtered using a third order low-pass Butterworth filter with a pass band of 3 hours and a stop band of period 2 hours in order to remove high frequency fluctuations in the data. The data were then subsampled at 1-hour intervals as required by the tidal analysis software. For consistency with the results from Foreman's analysis, the entire data set was smoothed with the low-pass filter and subsampled at hourly intervals.

Although the length of the record allows for the determination of several additional constituents, only five primary constituents are included: MSf, O_1, K_1, M_2 and S_2. The calculation was performed using a Rayleigh scaling factor of 2.0 for the July data set and 3.0 for the October data set. Both the axes of the representative tidal-ellipses and the corresponding Greenwich phase describe the main constituents of the tidal currents. The inclination of the ellipse indicates the angle the semi-major axis makes with the positive x-axis (15 and 22^o clockwise rotation for July and October

respectively). A positive value for the length of the semi-major axis indicates that the current rotates counter clockwise around the tidal ellipse, while a negative value indicates a clockwise rotation.

In addition to the summary information provided from the harmonic analysis, the time series were filtered using a least squared method to remove tidal signals at the MSf, O_1, K_1, M_2 and S_2 frequencies. The residual of this filter was then low-pass filtered with a third order Butterworth filter set to energy at periods shorter than 1.6 days.

Interpretation

Time series plots (Figures 3 and 4) show that the along-channel velocity is much greater than that across the channel, by a factor of 5-10 in speed. Covariance analysis was used to rotate the axis to maximize the along-channel velocity. This rotation was 15^o clockwise for the July/August deployment and 22^o for the October/November deployment. The degree of rotation did show some depth dependence but the difference between the surface and the bottom was less than 5^o. The mean difference between the two deployments may arise from differing oceanographic conditions or perhaps from the small difference in the location of the two deployments (which may differ by as much as 5-10 metres across the channel and perhaps 10-20 metres along the channel).

The power spectrum for currents in July/August shows clear peaks at 0.5 cycles per day (cpd), 1 cpd and 2 cpd (Figure 5). The M_2 tide shows remarkably little vertical structure in amplitude, even though it is baroclinic, while there does appear to be a minimum in the K_1 tide at mid-depths. The peak at 0.5 cpd is interesting as it is obviously not tidally forced. Energy at this period shows substantial depth dependence with a minimum centered at about 7 m. We explored coherence (Figure 6) between the current and different representations of the wind stress (amplitude, x and y components of stress, x and y components of stress in the rotated channel coordinates). The only significant coherence squared is at 0.5 cpd.

Tidal analysis was carried out on the u and v components in the rotated co-ordinate system. Although both components of velocity are included, clearly most of the

energy is in the along-channel component. The semi-diurnal components dominate, in particular the M_2 that has an amplitude of 34.7 cm (Table 3). The tables of the constituent analysis for the currents (Tables 4-17) and the plots of the tidal ellipses (Figures 7 and 8 for July/August) show that there is some depth dependence to the tidal current, although there is little depth dependence in the amplitude: 2.39 cm s^{-1} for M_2 at the surface and 1.95 cm s^{-1} at the bottom, in July. There is some evidence of baroclinicity in the M_2 tide but not in the K_1 tide. For July, the K_1 tide shows a phase difference from 1 to 14 m that is less than 12 degrees; for the M_2 tide the phase difference is roughly 163 degrees, indicating that the baroclinic response is primarily in mode 1. All the diurnal and semi-diurnal constituents show similar structure. As might be expected, given the change in stratification from July/August to October/November, with the increasing depth of the surface mixed layer and the reduced stratification between the upper and lower layers, there is no evidence of a baroclinic response in October/November. For this period, the phase difference from 3 to 13 m is less than 1^o for M_2 and 16^o for K_1.

The mean currents (Figure 9) show that the mean cross-channel current is approximately zero, as expected, but that there is significant depth dependence to the mean along-channel currents There is a mean outward surface current of about 4 cm s^{-1} near the surface, driven by the freshwater inflow from the Waterford River and sewage dumping. Surprisingly, the surface outflow is restricted to the top few metres of the water column, not very deep. There is also outflow at depth, below 10m, with inflow between 3 and 10m. The variance about these mean values is quite large (Figure 9). Plots of the spatial structure of the along-channel current (Figure 10) show that the spectral peak at 0.5 cpd is an inflow event covering most of the water column but is punctuated by outflow events near the bottom. There is not much evidence of energy at two-day periods (Figure 11) in the subtidal surface elevation. The outflow events which follow (or lead?) the inflows, are bottom intensified. The relationship between the inflows and outflows is unknown. The inflows begin near the bottom and spread to the surface as they develop. These observations, with uni-directional flow in the channel over most of the water column for day-long periods, raise questions about the cross-channel structure of the flow. The strong mean inflow at mid-depths is determined by this 0.5 cpd activity. The low-pass currents are also correlated with changes in water column particle concentration

as determined by the strength of the acoustic backscatter signal (Figure 13). Plots of the raw data for short periods (Figure 14) show that the low-frequency signal does in fact dominate and that the tidal signal is barely apparent. There is also a strong relationship between the backscatter intensity and the orientation and strength of the flow. For example, the bottom outflows around day 219 lead to substantial increases in the backscatter intensity, which rises off the bottom, matching the character of the bottom inflow event. This event shows that not all increases in backscatter intensity are associated with outflow events.

We also used the data to determine the transport over the sill, at subtidal and tidal periods. The transport from the current was determined by multiplying the current at each depth by the cross sectional channel area at that depth. We compared the results of this calculation with the observed net flux as determined from the rate of change of elevation in the harbour times the surface area of the harbour. At tidal periods we get generally reasonable agreement, within about 10% at the M_2 period. For the K_1 tide in July/August, the current data overpredicts the transport by about a factor of 1.5. The subtidal transport from the current data has a range of about –200 to + 200 m^3s^{-1}. The surface elevation data give a range in transport of –100 to + 100 m^3s^{-1}. The current transport calculation significantly overestimates the flux. While there may be some difficulties for the subtidal calculation, these differences are very large. That we get the M_2 correct confirms that the ADCP is measuring sensible currents through the channel. It is reasonable that we should get the transport for the strongest and clearest tidal constituent correct. That we overpredict the K_1 tide is probably because this tidal constituent is weaker and the tidal analysis of the current meter data is pulling in some of the energy at other periods. It is clear from the raw data (Figure 3) that there is a lot of non-tidal energy in the currents, much more than in the elevation data.

The cross-channel data are somewhat disappointing. We looked at the velocity from the two separate beams. For these data, we have not used averaged beam velocities, but instead use the speed from each beam separately. For about the first 50 metres, there is only a weak velocity signal in either beam (Figures 16 and 17). Beyond 50 m, however, the inward facing beam (pointing somewhat into the harbour) does show similar spectral peaks to the upward looking instrument, confirming that it is detecting

real currents (Figures 18 and 19). The other beam, which was pointing just outside of chain rock, does not show such a clear pattern and between 90 and 100 m shows a decline in spectral energy at almost all frequencies. We do not have a complete explanation for these observations but believe that the outward looking beam is being influenced by sidelobe interference between 90 and 100 m, causing a reduction in signal intensity. Separate plots of the velocity (Figures 16 and 17) reveal that in the far-field, beyond 80m, the two instruments show opposing velocities, perhaps indicating flow around the topographic features (Chain Rock) on the northern side of the channel.

There is very little thermal stratification in October, although there is a strong salinity gradient from the surface down to 5 m (Figure 20). Although the raw time series again show a predominance of along-channel flow (Figures 21 and 22) the October/November data reveal many differences from the observations in July/August. Note that the peak in the cross channel flow on day 297 is real and will be discussed later. As expected there is still energy at the tidal periods, the diurnal and the semi-diurnal, and there is also energy at the inertial period, roughly 1.5 cpd, as there is in July/August. The tidal peaks here are more dominant than in July/August. The wind-forced response at 0.5 cpd is again present in October/November although it is somewhat weaker than was observed in the July/August data (Figure 23). Coherence analysis again shows the relation between the wind and the currents at 0.5 cpd (Figure 24). One might expect the October/November wind-forced response to be stronger, given that wind forcing is more intense, however, the internal response may be stratification dependent. We suspect that the wind forcing at the two-day period is a result of forcing outside the harbour in the coastal waveguide in the Avalon Channel and that an internal Kelvin wave response is generated that rises up and enters the harbour, at a roughly two-day period (de Young et al. 1993, Davidson et al. 1999). Further modelling, and perhaps an expanded observation program, will be necessary to test this hypothesis.

The plots for the tidal ellipses show (Figures 25 and 26) the relative absence of vertical structure in the tidal signal discussed earlier. The mean currents in October/November (Figure 27) look much more like the expected two-layer circulation of an estuary with an outflow of about 4 cm s^{-1} at 3 m and inflow below 5 m depth with a peak inflow of over 6 cm s^{-1} at about 10m depth. Even a cursory glance at these plots

shows that there is more inflow than outflow, raising questions about the cross-channel structure of the along-channel flow. Stick plots of the velocity once again show that although the along-channel flow dominates, there is some vertical structure to the flow and bottom topographic steering is not uniform with depth (Figure 28). Surface elevation plots indicate a relation between strong wind events (e.g. just before day 290) and rising surface elevation (Figure 29).

The subtidal, along-channel currents show that the surface outflow is not steady but occurs in pulses of a few days duration that are linked to strong inflow events that extend from 8 m depth to the bottom (Figure 30). The surface outflow is restricted to the upper 5m with the strongest currents above 3m depth. Strong southwesterly winds do appear to be correlated with these exchange events, in particular, the strongest exchange around days 287-288 is correlated with the strongest wind event of the record corresponding to strong southerly winds that turn to southwesterly as they develop.

The backscatter plot (Figure 31) shows that at times there is some correlation between the inflow/outflow events and particle concentrations, but this is not consistent. Thus the first strong event does have the largest particle concentration, but is restricted to the surface waters. The other strong backscatter event is during the period from days 296-300. The structure of this event is more uniform with depth. Once again the raw data plots at hourly intervals (Figure 32) show that the low-frequency currents dominate. There is little energy at tidal periods, and a clear relationship between the strong outflow event around day 287.5 and the increase in the backscatter intensity near the surface, with no obvious connection with the wind, which lags this event.

The October/November tidal transport calculations from the currents and elevation agree to within 10% for both the M_2 and K_1 tides. It is apparent from the time series that the October data (Figure 21) shows much stronger tidal transport, relative to the subtidal, than do the July data (Figure 3). The subtidal transport calculations again show poor agreement between the currents and elevation (Figure 33). Not only is there poor agreement but the currents overpredict the amplitude by about a factor of three. The lower panel in Figure 33 shows that the total transport as determined from our current meter data is always into the harbour. This result is not physically sensible and indicates that there is a strong gradient in the cross-channel structure of the flow. The transport as

determined from the observed surface elevation (Figure 33) shows that the maximum transport is roughly 10 $m^3 s^{-1}$, a much more reasonable result and one that is expected given that the mean freshwater inflow in this system is of order 1 $m^3 s^{-1}$.

What about the residence time for water in the Harbour? If we take the mean depth as about 12-15 m then the total volume of the harbour is about 1.5 x 10^7 m^3. The maximum transport in July/August as calculated from the surface elevation is about 5 $m^3 s^{-1}$, which would correspond to an exchange time of 34 days for all the harbour water. If we take the maximum transport from the current calculations, then we get an exchange time of less than 2-3 days. The surface elevation from October/November gives a maximum transport of 10 $m^3 s^{-1}$ giving an exchange time of about 17 days. The current transport from October/November gives an exchange time of less than 2-3 days. The surface elevation transport result probably provides an exchange time that is too long, while the current determined transport provides an exchange time that is too short. Water in the harbour is not completely mixed. Water in the northeastern half of the harbour probably has a much shorter exchange time than water in the southwestern half. In particular, surface water in the northeastern corner probably has the shortest residence time of all the water in the harbour. The average exchange period for the harbour is 5-15 days, perhaps even shorter during periods of particularly strong forcing.

But what about the effect of tidal exchange? The strongest tides in the system are the semidiurnal tides, the M_2 and S_2, with amplitudes of roughly 2-4 cm s^{-1}. The semi-diurnal tidal transport through the narrows is therefore about 50 $m^3 s^{-1}$. During flood tide this corresponds to an inflow of somewhat less than 10% of the total volume of the harbour giving an exchange time of about 6-7 days. Combining the subtidal and tidal exchange estimates suggests that the real exchange rate is probably closer to the five-day period than it is to the fifteen-day period. This shorter exchange rate is consistent with the observed high oxygen levels in the surface and the deeper water of the harbour.

The large cross-channel velocity that appears around day 297 and stands out in Figure 22 is apparently real and is not an artifact. Close inspection of the data for this period reveals that there is strong inflow and outflow, beginning just after 3:00 PM local time on 25 October. The currents are so strong that the instrument is knocked off its location and its orientation disrupted, as shown by large, abrupt changes in the internal

inclination sensors. The current during the period is strongly into and then out of the channel, oscillating with a twenty minute period (Figure 34), or perhaps less since the sampling period is twenty minutes. There is no response the elevation in the harbour, nor is there anything obvious in either the wind time series or the temperature data. These data show that the winds in St. John's were in fact quite light. At the same time large seiches, or harbour waves, were generated in Petty Harbour, Port Rexton and Little Catalina (B. Whiffen, Environment Canada, personal communication). The seiche in Petty Harbour was several metres in amplitude with a period of tens of minutes, running over the dock, and persisting for several hours.

The event in St. John's harbour did not generate a seiche in the basin but did have some substantial effect on the circulation in the Narrows. Indeed, the backscatter time series (Figure 34) shows that particle concentrations dramatically increased throughout the water column, with the greatest intensity at the bottom. This event in the backscatter took several hours to dissipate. These events could have been forced by some external wave, perhaps a tsunami associated with a shelf-break slumping event or the passage of a dissipating hurricane.

Summary

These data tell us a number of interesting things about the transport through the Narrows into St. John's harbour:

(1) Tidal circulation is not particularly dominant.
(2) The summer circulation is at least as strong as that observed in the late fall, perhaps stronger.
(3) Even during the summer, the wind forced transport at a period of roughly 2 days generates large transports and large velocities through the narrows.
(4) Surface elevation shows substantial subtidal variability but the response at 2 days period is primarily baroclinic and not barotropic.
(5) We estimate the mean residence time of water in the Harbour to be roughly 5-10 days.

(6) Current shear across the channel is substantial, in particular at subtidal periods, and the strong inflow that we observe in the centre of the channel must be balanced by strong outflows along the sides of the channel.

We believe that the shape and position of the Narrows is important in determining the currents that we report on as measured here at the western end of the Narrows (Figure 1). Note that the Narrows is 2-3 times wider at its eastern end than it is to the west where it attaches to the harbour. Water flowing in through this channel accelerates as it enters the harbour, thereby leading to the strong jet that we see on inflow events. The opposite will happen on outflow and it must be that the strong outflow is concentrated along the sides of the channel away from the centre of the channel. A mooring program with additional instruments across the channel is required to close the transport over the sill of St. John's Harbour.

References:

deYoung, B., Otterson, T. and R. Greatbatch. 1993. The local and non-local response of Conception Bay to wind forcing. *J. Phys. Ocean*., **23**, 2636-2649.

Davidson, F. , Greatbatch, R. and B. deYoung. 2000. Asymmetry in the response of a stratified coastal embayment to wind forcing. *J. Geophys. Res*. (in press).

Foreman, M. Manual for Tidal Heights Analysis and Prediction, Pacific Marine Science Report 78-6, Institute of Ocean Sciences, Patricia Bay, Victoria B.C., (1977)

July Data Set

Table 2: Summary Statistics of ADCP currents from mid-channel station (see Figure 1).

Depth (m)	Component	Max (cm s^{-1})	Min (cm s^{-1})	Mean (cm s^{-1})	Std (cm s^{-1})
1	v	11.76	0.01	-0.81	2.39
	u	35.21	0.00	3.34	9.15
2	v	9.31	0.00	-0.69	1.87
	u	32.94	0.00	1.53	9.01
3	v	6.87	0.01	-0.83	1.80
	u	33.10	0.00	-1.11	8.50
4	v	8.13	0.00	-1.06	1.74
	u	31.96	0.03	-3.11	7.65
5	v	7.80	0.01	-1.23	1.55
	u	35.01	0.01	-4.48	7.04
6	v	7.13	0.01	-1.41	1.55
	u	34.93	0.01	-5.06	6.86
7	v	8.10	0.00	-1.43	1.62
	u	37.86	0.00	-5.02	7.01
8	v	8.11	0.00	-1.41	1.64
	u	37.35	0.00	-4.27	7.58
9	v	7.84	0.00	-1.48	1.59
	u	40.37	0.02	-2.82	8.56
10	v	6.97	0.00	-1.63	1.58
	u	41.86	0.01	-1.03	9.58
11	v	6.86	0.02	-1.69	1.57
	u	41.99	0.03	0.94	10.43
12	v	8.15	0.01	-1.96	1.75
	u	41.55	0.02	2.74	11.02
13	v	8.81	0.01	-2.04	1.90
	u	40.12	0.04	4.41	11.33
14	v	10.00	0.00	-1.76	1.96
	u	37.54	0.02	5.69	11.55

Table 3: Tidal height analysis of surface elevation data measured at the head of the harbour.

Name	Frequency	Amplitude	G. Phase
Z_0	0.00000000	83.30	0.00
MSf	0.00282193	1.09	10.9
O_1	0.03873065	6.63	320.3
K_1	0.04178075	9.57	130.5
M_2	0.08051140	34.67	95.0
S_2	0.08333334	12.41	269.9

The main tidal constituents of the July data set from the mid-channel station (Figure 1).

Table 4: Main Constituents of the Tidal Currents, July: Depth 1 m.

Name	Frequency	Major Axis ($cm\ s^{-1}$)	Minor Axis ($cm\ s^{-1}$)	Inclination	G. Phase
Z_0	0.00000000	3.30	0.00	166.2	180.0
MSf	0.00282193	0.50	-0.21	163.5	70.5
O_1	0.03873065	0.38	0.33	59.2	351.3
K_1	0.04178075	2.38	-0.06	1.4	144.3
M_2	0.08051140	2.39	0.16	5.3	307.1
S_2	0.08333334	2.00	0.05	176.9	186.1

Table 5: Main Constituents of the Tidal Currents, July: Depth 2 m.

Name	Frequency	Major Axis ($cm\ s^{-1}$)	Minor Axis ($cm\ s^{-1}$)	Inclination	G. Phase
Z_0	0.00000000	1.58	0.00	154.2	180.0
MSf	0.00282193	1.16	-0.12	6.3	273.5
O_1	0.03873065	0.32	-0.11	8.7	181.9
K_1	0.04178075	2.40	-0.07	1.0	151.2
M_2	0.08051140	2.58	0.02	3.0	341.4
S_2	0.08333334	2.22	-0.17	176.2	203.3

Table 6: Main Constituents of the Tidal Currents, July: Depth 3 m.

Name	Frequency	Major Axis ($cm\ s^{-1}$)	Minor Axis ($cm\ s^{-1}$)	Inclination	G. Phase
Z_0	0.00000000	1.50	0.00	33.1	180.0
MSf	0.00282193	1.39	-0.07	0.8	278.4
O_1	0.03873065	0.54	0.03	176.5	19.6
K_1	0.04178075	2.16	-0.09	10.7	153.4
M_2	0.08051140	2.83	0.15	5.3	342.3
S_2	0.08333334	2.19	-0.17	178.3	203.3

Table 7: Main Constituents of the Tidal Currents, July: Depth 4 m.

Name	Frequency	Major Axis ($cm\ s^{-1}$)	Minor Axis ($cm\ s^{-1}$)	Inclination	G. Phase
Z_0	0.00000000	3.43	0.00	17.8	180.0
MSf	0.00282193	1.42	0.01	1.5	275.4
O_1	0.03873065	0.52	0.12	165.4	21.6
K_1	0.04178075	1.81	0.06	14.0	143.2
M_2	0.08051140	2.92	0.06	9.5	342.2
S_2	0.08333334	2.32	0.05	2.9	23.3

Table 8: Main Constituents of the Tidal Currents, July: Depth 5 m.

Name	Frequency	Major Axis (cm s^{-1})	Minor Axis (cm s^{-1})	Inclination	G. Phase
Z_0	0.00000000	4.77	0.000	14.8	180.0
MSf	0.00282193	1.30	-0.04	2.4	262.9
O_1	0.03873065	0.43	0.09	0.1	231.7
K_1	0.04178075	1.41	0.02	16.7	137.5
M_2	0.08051140	2.91	0.05	10.1	339.6
S_2	0.08333334	2.30	0.03	9.3	19.1

Table 9: Main Constituents of the Tidal Currents, July: Depth 6 m.

Name	Frequency	Major Axis (cm s^{-1})	Minor Axis (cm s^{-1})	Inclination	G. Phase
Z_0	0.00000000	5.34	0.00	15.1	180.0
MSf	0.00282193	1.18	0.03	2.4	255.3
O_1	0.03873065	0.33	0.05	19.0	306.5
K_1	0.04178075	0.96	-0.10	6.3	120.1
M_2	0.08051140	2.90	0.07	11.3	334.4
S_2	0.08333334	2.11	0.12	11.7	15.6

Table 10: Main Constituents of the Tidal Currents, July: Depth 7 m.

Name	Frequency	Major Axis (cm s^{-1})	Minor Axis (cm s^{-1})	Inclination	G. Phase
Z_0	0.00000000	5.29	0.00	15.7	180.0
MSf	0.00282193	0.94	0.04	4.0	250.8
O_1	0.03873065	0.64	-0.07	15.6	330.8
K_1	0.04178075	0.40	-0.18	13.7	101.5
M_2	0.08051140	2.90	0.09	10.5	332.7
S_2	0.08333334	1.90	0.18	10.0	11.0

Table 11: Main Constituents of the Tidal Currents, July: Depth 8 m.

Name	Frequency	Major Axis (cm s^{-1})	Minor Axis (cm s^{-1})	Inclination	G. Phase
Z_0	0.00000000	4.54	0.00	18.2	180.0
MSf	0.00282193	0.84	0.06	5.3	240.6
O_1	0.03873065	0.51	-0.05	15.5	333.6
K_1	0.04178075	0.34	-0.11	30.5	345.9
M_2	0.08051140	2.80	0.08	7.9	331.2
S_2	0.08333334	1.75	0.11	4.6	11.0

Table 12: Main Constituents of the Tidal Currents, July: Depth 9 m.

Name	Frequency	Major Axis (cm s^{-1})	Minor Axis (cm s^{-1})	Inclination	G. Phase
Z_0	0.00000000	3.22	0.00	27.3	180.0
MSf	0.00282193	0.74	0.03	9.8	241.6
O_1	0.03873065	0.32	-0.15	179.7	175.8
K_1	0.04178075	0.74	-0.09	179.2	170.3
M_2	0.08051140	2.76	0.08	7.0	331.2
S_2	0.08333334	1.69	0.19	9.5	14.9

Table 13: Main Constituents of the Tidal Currents, July: Depth 10 m.

Name	Frequency	Major Axis (cm s^{-1})	Minor Axis (cm s^{-1})	Inclination	G. Phase
Z_0	0.00000000	1.94	0.00	56.0	180.0
MSf	0.00282193	0.80	-0.09	13.6	248.3
O_1	0.03873065	0.26	0.08	17.9	95.3
K_1	0.04178075	0.97	-0.12	176.4	163.8
M_2	0.08051140	2.76	0.09	3.1	330.1
S_2	0.08333334	1.58	0.17	7.0	18.1

Table 14: Main Constituents of the Tidal Currents, July: Depth 11 m.

Name	Frequency	Major Axis (cm s^{-1})	Minor Axis (cm s^{-1})	Inclination	G. Phase
Z_0	0.00000000	1.87	0.00	118.8	180.0
MSf	0.00282193	0.70	-0.20	11.9	246.7
O_1	0.03873065	0.46	-0.02	8.8	106.9
K_1	0.04178075	1.20	-0.01	172.8	165.3
M_2	0.08051140	2.65	0.07	179.6	149.0
S_2	0.08333334	1.45	0.17	2.3	18.1

Table 15: Main Constituents of the Tidal Currents, July: Depth 12 m.

Name	Frequency	Major Axis (cm s^{-1})	Minor Axis (cm s^{-1})	Inclination	G. Phase
Z_0	0.00000000	3.36	0.00	144.6	180.0
MSf	0.00282193	0.61	-0.12	13.3	240.9
O_1	0.03873065	0.53	-0.02	175.3	300.8
K_1	0.04178075	1.25	-0.18	165.1	160.9
M_2	0.08051140	2.42	0.07	0.3	328.3
S_2	0.08333334	1.49	0.11	2.8	22.1

Table 16: Main Constituents of the Tidal Currents, July: Depth 13 m.

Name	Frequency	Major Axis (cm s^{-1})	Minor Axis (cm s^{-1})	Inclination	G. Phase
Z_0	0.00000000	4.86	0.00	155.3	180.0
MSf	0.00282193	0.52	0.06	3.9	247.9
O_1	0.03873065	0.41	-0.01	147.5	299.7
K_1	0.04178075	1.06	-0.21	166.1	143.5
M_2	0.08051140	2.17	0.06	177.7	147.6
S_2	0.08333334	1.44	0.05	7.9	20.4

Table 17: Main Constituents of the Tidal Currents, July: Depth 14 m

Name	Frequency	Major Axis (cm s^{-1})	Minor Axis (cm s^{-1})	Inclination	G. Phase
Z_0	0.00000000	5.94	0.00	162.7	180.0
MSf	0.00282193	0.43	0.10	10.9	261.6
O_1	0.03873065	0.36	0.22	119.0	274.7
K_1	0.04178075	0.84	-0.11	163.1	132.1
M_2	0.08051140	1.94	0.20	178.6	145.9
S_2	0.08333334	1.67	0.60	7.6	15.5

October Data Set

Table 18: Summary statistics of currents from the mid-channel station.

Depth (m)	Component	Max (cm s^{-1})	Min (cm s^{-1})	Mean (cm s^{-1})	Std (cm s^{-1})
3	v	17.74	0.00	-0.11	1.93
	u	30.91	0.02	4.42	5.93
4	v	19.34	0.01	-0.15	1.93
	u	27.26	0.00	1.93	5.73
5	v	20.13	0.00	-0.39	2.16
	u	21.90	0.00	-0.27	5.22
6	v	22.03	0.00	-0.73	2.29
	u	21.39	0.01	-2.28	4.71
7	v	21.06	0.00	-1.04	2.22
	u	21.96	0.04	-3.83	4.59
8	v	23.50	0.00	-1.62	2.06
	u	21.50	0.01	-5.41	4.90
9	v	22.42	0.01	-1.77	2.16
	u	24.33	0.01	-6.08	5.52
10	v	23.57	0.00	-1.94	2.18
	u	27.00	0.00	-6.43	6.01
11	v	24.72	0.00	-1.91	2.18
	u	28.42	0.03	-6.42	6.43
12	v	22.90	0.00	-1.80	2.18
	u	28.41	0.11	-6.37	6.68
13	v	23.39	0.01	-1.63	2.10
	u	27.80	0.01	-6.10	6.84
14	v	21.74	0.00	-1.30	1.94
	u	26.32	0.03	-5.71	6.92
15	v	18.65	0.00	-0.95	1.81
	u	25.93	0.03	-5.28	6.99

Table 19: Tidal height analysis from surface elevations measured at the head of the harbour.

Name	Frequency	Amplitude	G. Phase
Z_0	0.00000000	89.00	0.00
MSf	0.00282193	7.44	219.0
O_1	0.03873065	5.41	21.83
K_1	0.04178075	7.16	109.55
M_2	0.08051140	36.30	167.57
S_2	0.08333334	15.42	244.31

The main tidal constituents of the October data set from the mid-channel station (Figure1).

Table 20: Main Constituents of the Tidal Currents, October: Depth 3 m.

Name	Frequency	Major Axis (cm s^{-1})	Minor Axis (cm s^{-1})	Inclination	G. Phase
Z_0	0.00000000	4.31	0.00	178.0	180.0
MSf	0.00282193	1.66	0.21	175.1	357.6
O_1	0.03873065	1.10	-0.09	173.4	202.2
K_1	0.04178075	1.34	0.14	173.1	209.1
M_2	0.08051140	3.74	-0.52	2.5	7.7
S_2	0.08333334	1.76	0.13	1.1	39.0

Table 21: Main Constituents of the Tidal Currents, October: Depth 4 m.

Name	Frequency	Major Axis (cm s^{-1})	Minor Axis (cm s^{-1})	Inclination	G. Phase
Z_0	0.00000000	1.83	0.00	173.9	180.0
MSf	0.00282193	1.38	0.34	5.8	208.8
O_1	0.03873065	0.96	-0.03	179.6	200.4
K_1	0.04178075	1.47	-0.07	179.9	220.5
M_2	0.08051140	4.19	-0.36	4.5	12.6
S_2	0.08333334	1.69	0.04	15.2	38.3

Table 22: Main Constituents of the Tidal Currents, October: Depth 5 m.

Name	Frequency	Major Axis (cm s^{-1})	Minor Axis (cm s^{-1})	Inclination	G. Phase
Z_0	0.00000000	0.60	0.00	52.4	180.0
MSf	0.00282193	1.35	0.18	25.5	237.8
O_1	0.03873065	0.72	0.07	9.0	27.2
K_1	0.04178075	1.21	-0.20	4.2	44.8
M_2	0.08051140	4.36	-0.16	8.1	14.9
S_2	0.08333334	1.63	0.07	20.6	24.7

Table 23: Main Constituents of the Tidal Currents, October: Depth 6 m.

Name	Frequency	Major Axis (cm s^{-1})	Minor Axis (cm s^{-1})	Inclination	G. Phase
Z_0	0.00000000	2.49	0.00	18.6	180.0
MSf	0.00282193	1.39	-0.11	35.6	265.5
O_1	0.03873065	0.52	0.01	8.3	36.1
K_1	0.04178075	0.83	-0.09	4.6	57.4
M_2	0.08051140	4.48	-0.08	12.3	13.2
S_2	0.08333334	1.65	0.08	20.8	14.1

Table 24: Main Constituents of the Tidal Currents, October: Depth 7 m.

Name	Frequency	Major Axis (cm s^{-1})	Minor Axis (cm s^{-1})	Inclination	G. Phase
Z_0	0.00000000	4.05	0.00	15.8	180.0
MSf	0.00282193	1.34	-0.40	34.3	284.7
O_1	0.03873065	0.56	-0.09	25.6	66.8
K_1	0.04178075	0.61	-0.16	169.1	275.3
M_2	0.08051140	4.61	-0.09	13.0	13.4
S_2	0.08333334	1.69	0.01	20.3	7.6

Table 25: Main Constituents of the Tidal Currents, October: Depth 8 m.

Name	Frequency	Major Axis (cm s^{-1})	Minor Axis (cm s^{-1})	Inclination	G. Phase
Z_0	0.00000000	5.69	0.00	16.8	180.0
MSf	0.00282193	1.31	-0.39	17.2	312.6
O_1	0.03873065	0.59	-0.30	179.7	274.0
K_1	0.04178075	0.72	0.15	5.7	140.4
M_2	0.08051140	4.25	-0.12	12.5	13.0
S_2	0.08333334	1.69	0.04	21.1	4.6

Table 26: Main Constituents of the Tidal Currents, October: Depth 9 m.

Name	Frequency	Major Axis (cm s^{-1})	Minor Axis (cm s^{-1})	Inclination	G. Phase
Z_0	0.00000000	6.35	0.00	16.4	180.0
MSf	0.00282193	1.41	-0.39	11.4	328.8
O_1	0.03873065	0.70	-0.14	170.8	305.9
K_1	0.04178075	1.040	0.27	9.3	164.7
M_2	0.08051140	4.11	-0.17	13.3	11.5
S_2	0.08333334	1.69	0.04	20.2	4.6

Table 27: Main Constituents of the Tidal Currents, October: Depth 10 m.

Name	Frequency	Major Axis (cm s^{-1})	Minor Axis (cm s^{-1})	Inclination	G. Phase
Z_0	0.00000000	6.72	0.00	16.9	180.0
MSf	0.00282193	1.59	-0.26	9.3	338.6
O_1	0.03873065	0.61	-0.08	176.6	315.1
K_1	0.04178075	1.18	0.11	13.9	178.2
M_2	0.08051140	3.94	-0.09	13.2	12.5
S_2	0.08333334	1.56	0.05	15.7	4.9

Table 28: Main Constituents of the Tidal Currents, October: Depth 11 m.

Name	Frequency	Major Axis (cm s^{-1})	Minor Axis (cm s^{-1})	Inclination	G. Phase
Z_0	0.00000000	6.67	0.00	16.9	180.0
MSf	0.00282193	1.67	-0.14	2.5	348.5
O_1	0.03873065	0.66	0.00	0.6	140.5
K_1	0.04178075	1.10	0.08	8.1	181.6
M_2	0.08051140	3.95	-0.09	9.8	11.3
S_2	0.08333334	1.43	-0.03	13.0	6.9

Table 29: Main Constituents of the Tidal Currents, October: Depth 12 m.

Name	Frequency	Major Axis (cm s^{-1})	Minor Axis (cm s^{-1})	Inclination	G. Phase
Z_0	0.00000000	6.57	0.00	16.2	180.0
MSf	0.00282193	1.69	-0.16	179.9	179.6
O_1	0.03873065	0.56	0.01	179.5	316.3
K_1	0.04178075	0.98	0.06	17.4	180.4
M_2	0.08051140	3.87	-0.24	8.1	9.8
S_2	0.08333334	1.40	-0.08	8.9	9.9

Table 30: Main Constituents of the Tidal Currents, October: Depth 13 m

Name	Frequency	Major Axis (cm s^{-1})	Minor Axis (cm s^{-1})	Inclination	G. Phase
Z_0	0.00000000	6.24	0.00	15.5	180.0
MSf	0.00282193	1.85	-0.13	175.8	185.4
O_1	0.03873065	0.50	0.03	178.6	325.5
K_1	0.04178075	0.87	0.03	21.2	193.6
M_2	0.08051140	3.81	-0.22	5.5	8.3
S_2	0.08333334	1.40	-0.06	2.3	9.4

Table 31: Main Constituents of the Tidal Currents, October: Depth 14 m

Name	Frequency	Major Axis (cm s^{-1})	Minor Axis (cm s^{-1})	Inclination	G. Phase
Z_0	0.00000000	5.73	0.00	13.3	180.0
MSf	0.00282193	1.96	-0.11	177.5	193.1
O_1	0.03873065	0.46	0.05	168.4	322.2
K_1	0.04178075	0.75	0.03	15.8	192.1
M_2	0.08051140	3.50	-0.23	4.0	7.4
S_2	0.08333334	1.41	-0.13	179.4	192.7

Table 32: Main Constituents of the Tidal Currents, October: Depth 15 m

Name	Frequency	Major Axis (cm s^{-1})	Minor Axis (cm s^{-1})	Inclination	G. Phase
Z_0	0.00000000	5.23	0.00	10.5	180.0
MSf	0.00282193	2.12	-0.14	0.7	21.3
O_1	0.03873065	0.35	0.06	6.5	158.2
K_1	0.04178075	0.72	-0.04	5.8	184.1
M_2	0.08051140	3.29	-0.17	4.3	7.1
S_2	0.08333334	1.24	-0.05	174.9	192.2

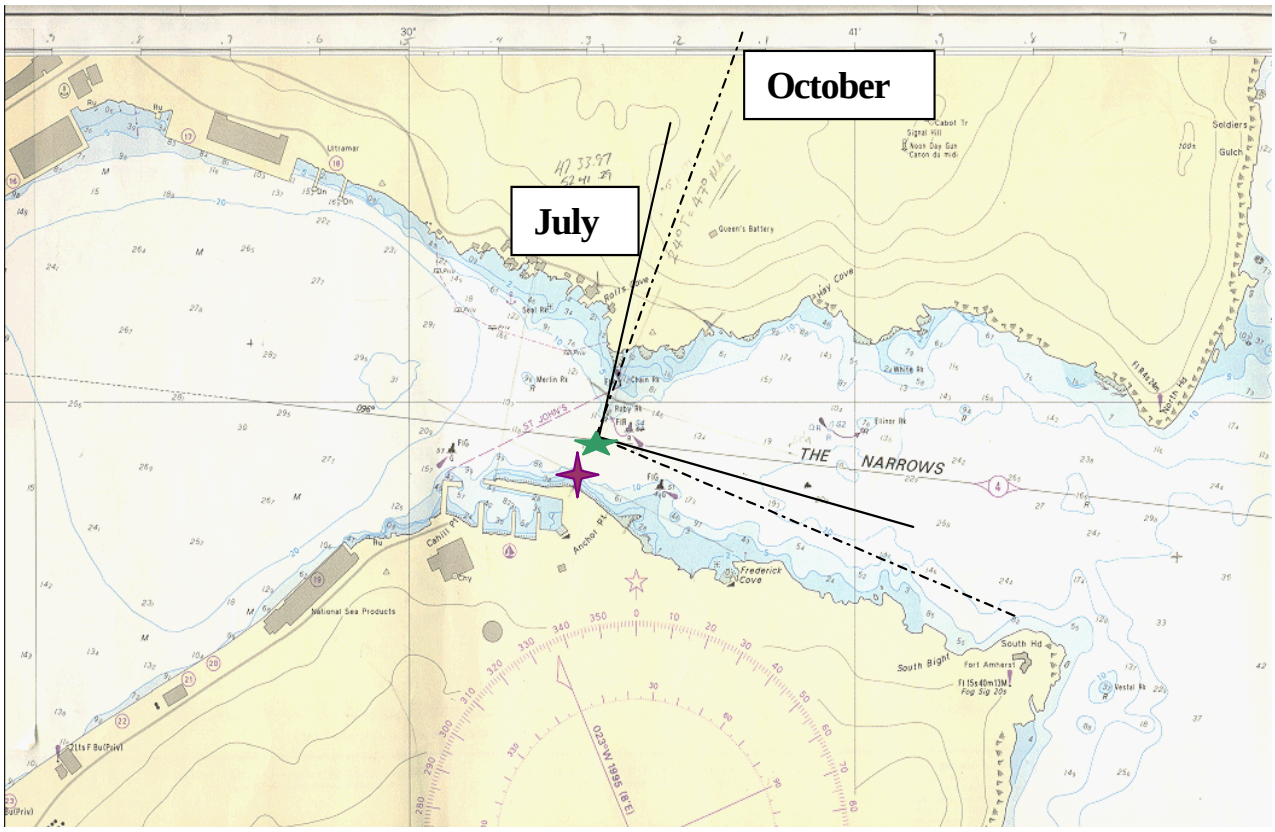

Figure 1: Location of upward looking ADCP (green star), and cross-channel ADCP (July only, purple star). Included are the orientation of the axes for the rotated frame of reference for both July and October. The mid-channel station for October was also at the green-star position.

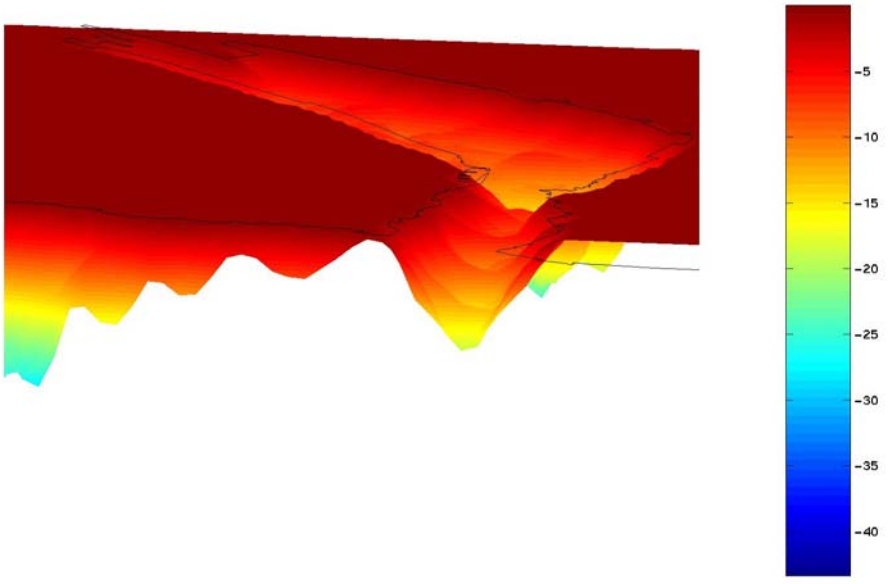

Figure 2: Three dimensional topographic view of St. John's Harbour. The shoreline and docks are overlaid in black. The depth scale is in metres, with the land set to zero and the harbour/sill bottom at negative depths.

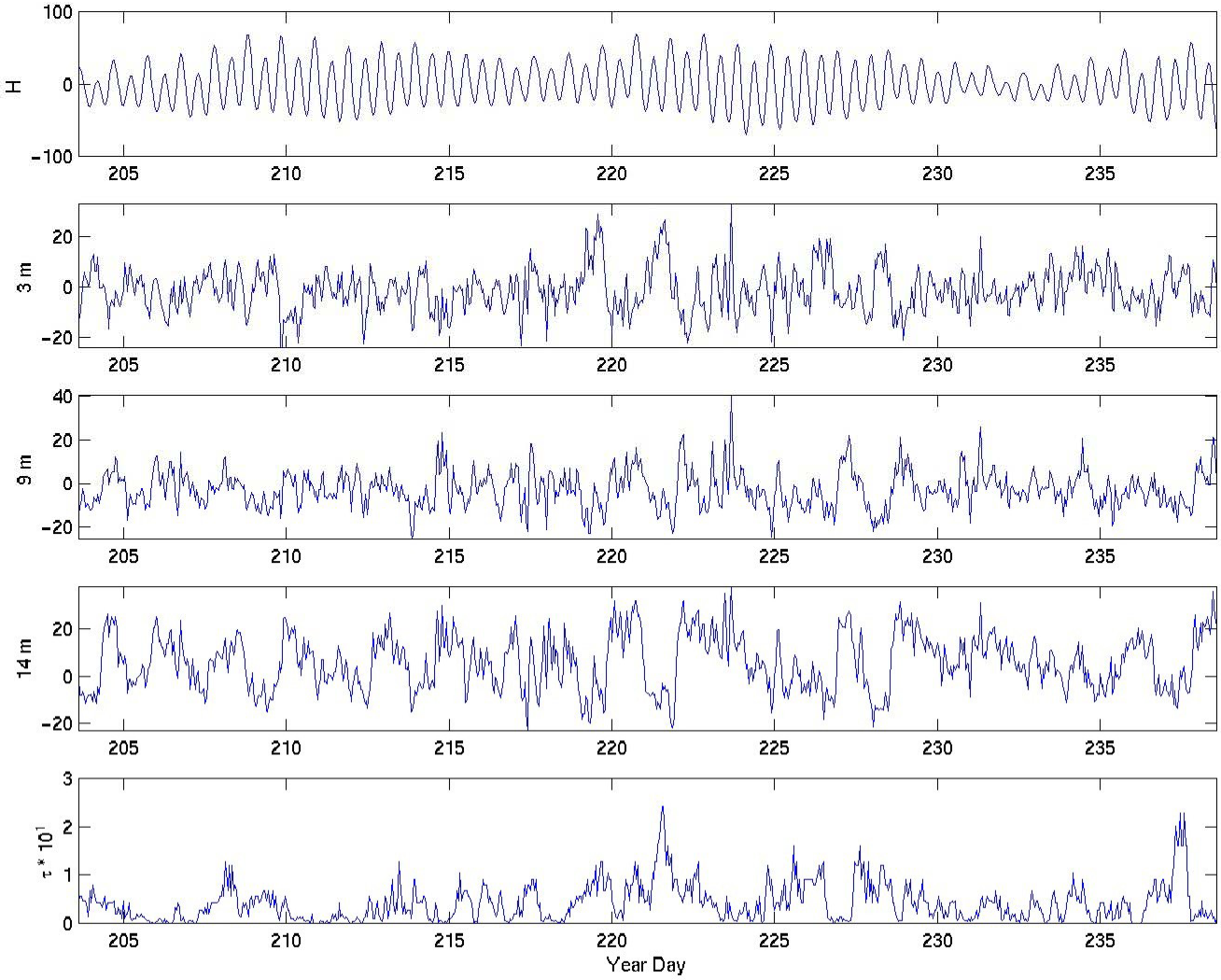

Figure 3: Time series of surface elevation, current velocity along the channel axis (15 degrees from earth axes) at 3, 9 and 14 metres, and the magnitude of the wind stress. The surface elevation is measured in cm, and the current velocities are in cm s^{-1}. The wind stress amplitude is measured in 0.1 N m^{-2}.

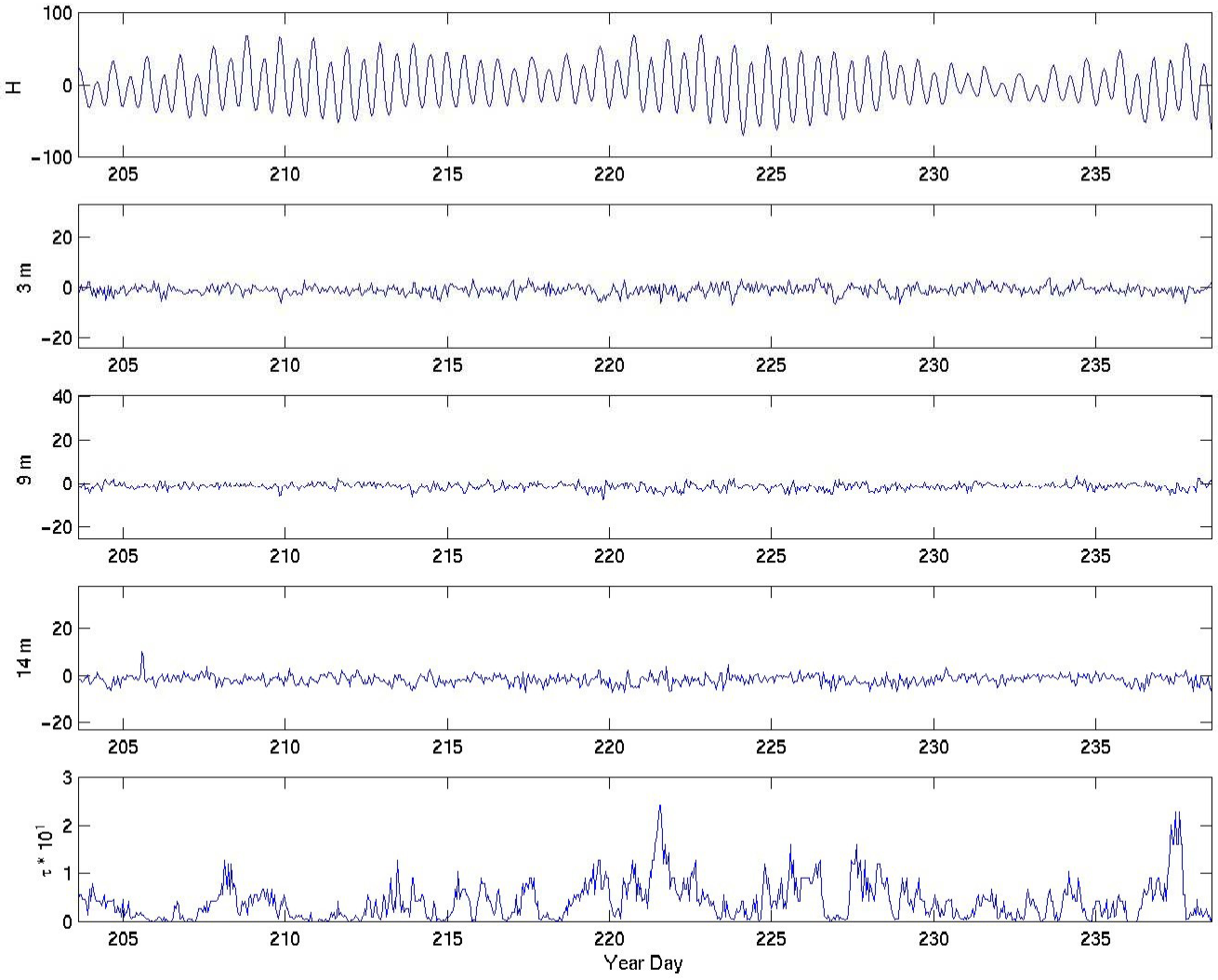

Figure 4: Time series of surface elevation, current velocity across the channel axis (15 degrees from earth axes) at 3, 5 and 14 metres, and the magnitude of the wind stress. The surface elevation is measured in cm, and the current velocities are in cm s^{-1}. The wind stress amplitude is measured in 0.1 N m^{-2}.

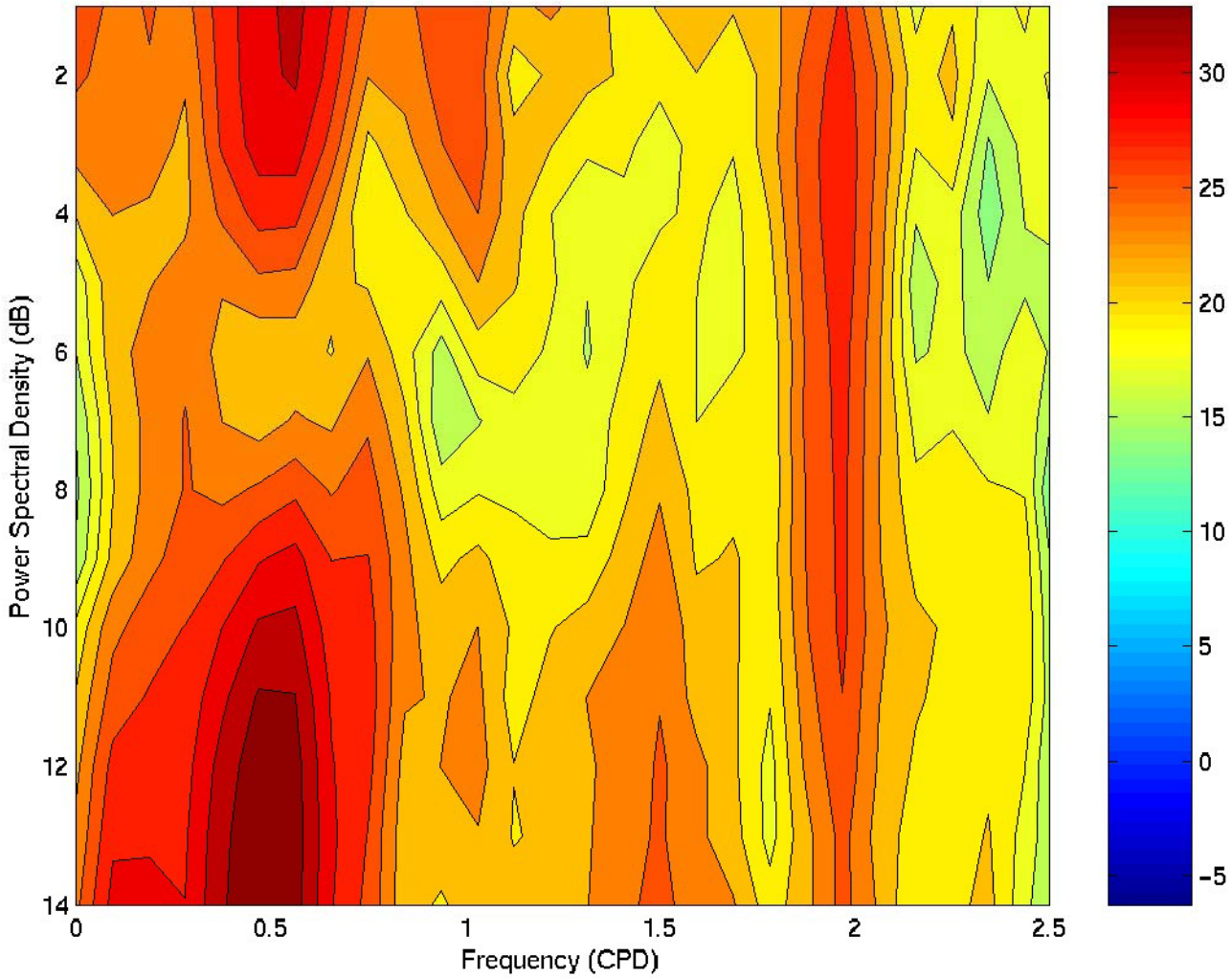

Figure 5: The power spectral density in deciBels for the along channel component of velocity. The frequency is measured in cycles per day, and the depth is in metres. These spectra have 9 degrees of freedom.

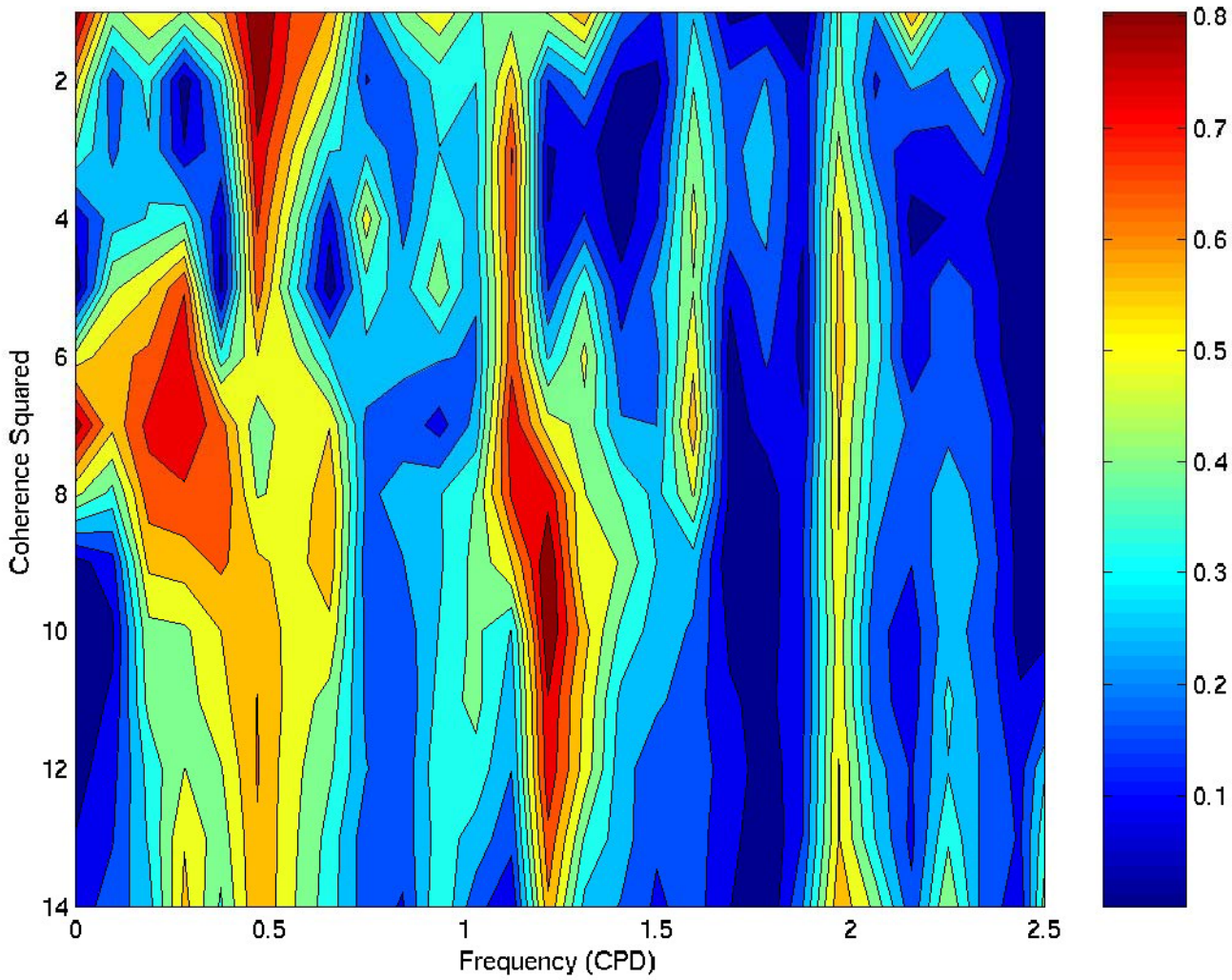

Figure 6: The coherence squared between the East-West component of wind stress and the along channel current velocity. The coherence squared has 9 degrees of freedom.

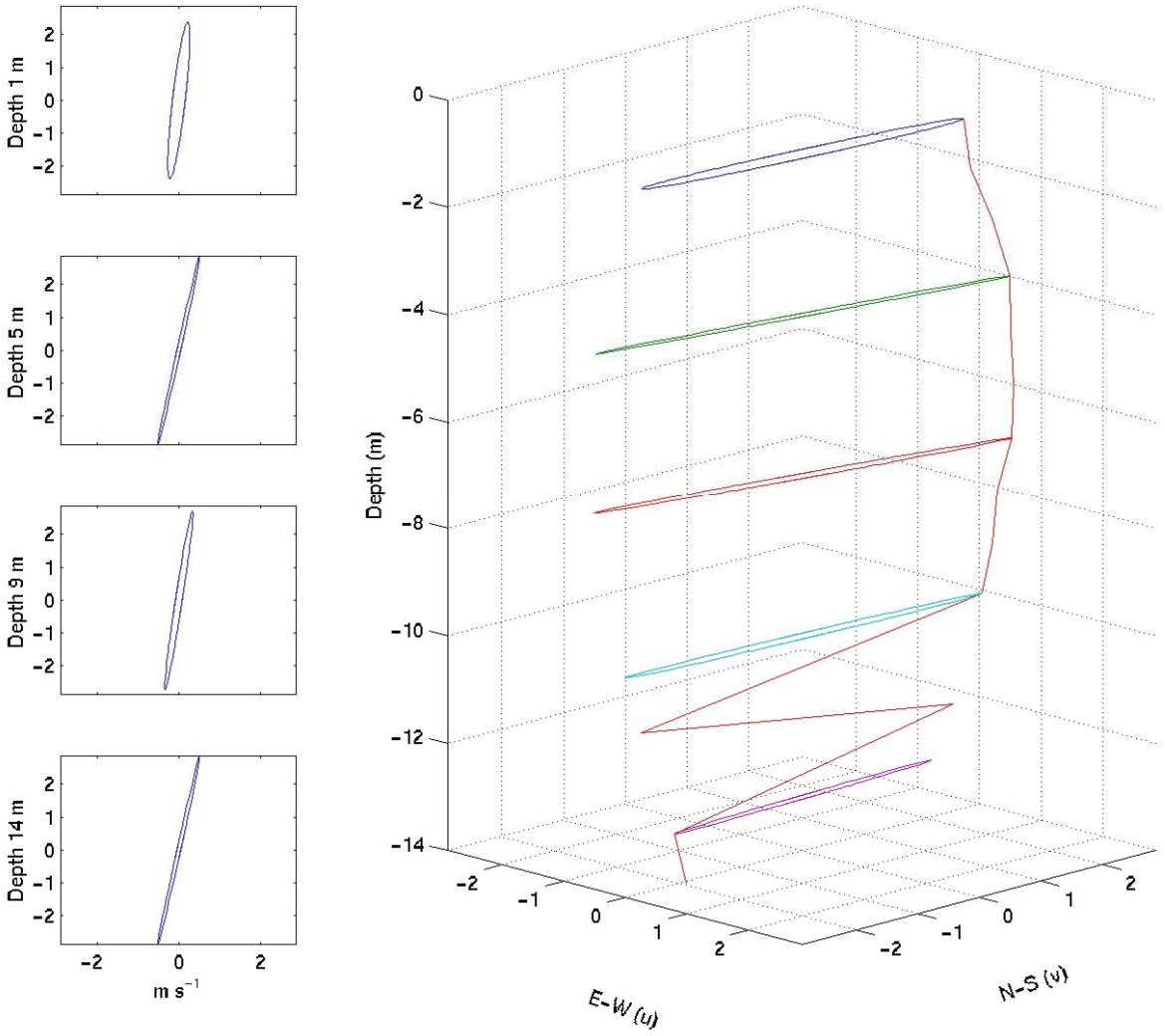

Figure 7: The major and minor axes of the M_2 tidal constituent. The axes represent velocities measured in cm s^{-1}. For the three dimensional plot of the tidal ellipses, the red line represents the inclination of each tidal ellipse at depth, with respect to the rotated axes. Here E-W is the along-channel axis.

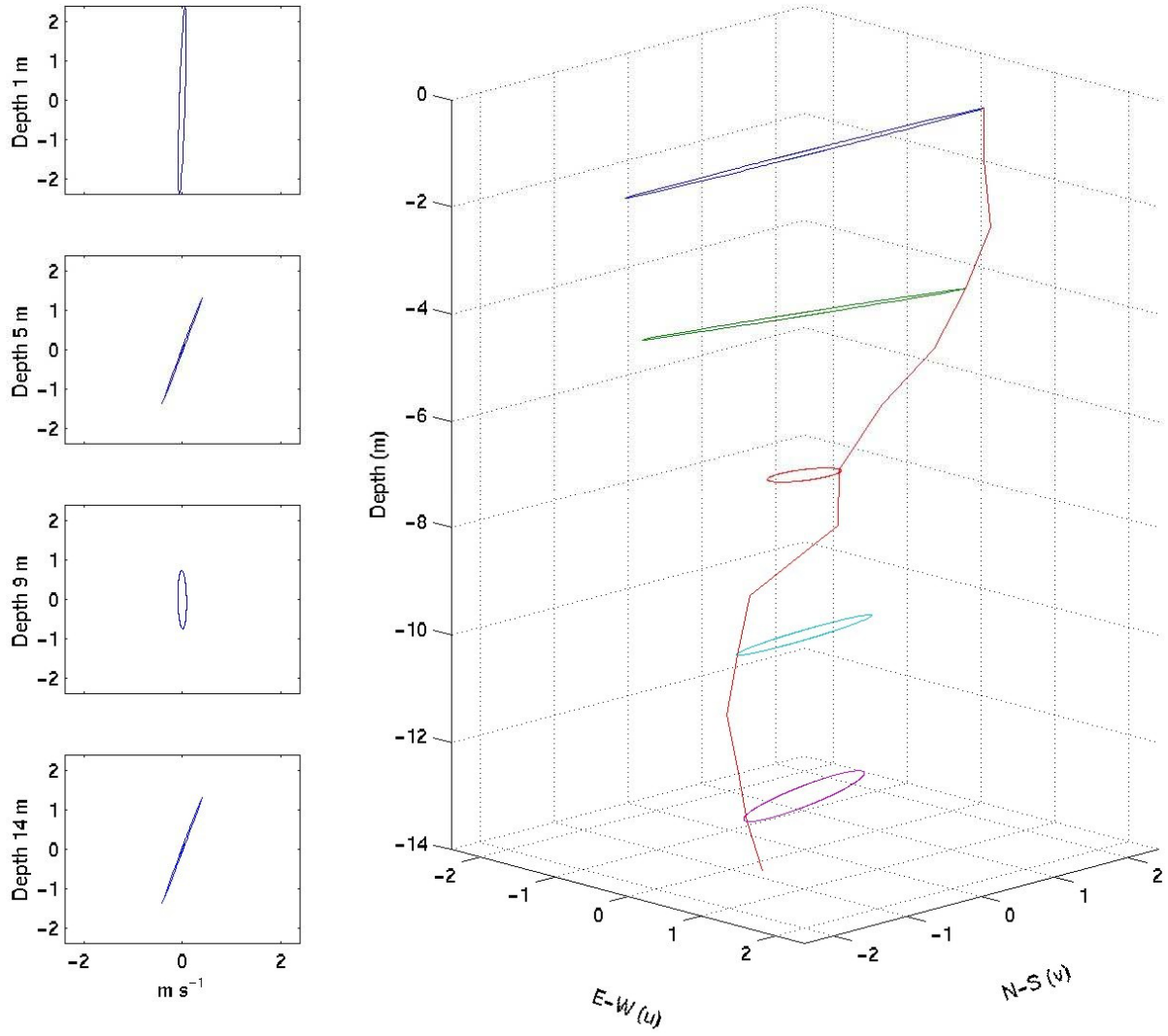

Figure 8: The major and minor axes of the K_1 tidal constituent. The axes represent velocities measured in cm s $^{-1}$. For the three dimensional plot of the tidal ellipses, the red line represents the inclination of each tidal ellipse at depth, with respect to the rotated axes. Here E-W is the along-channel axis.

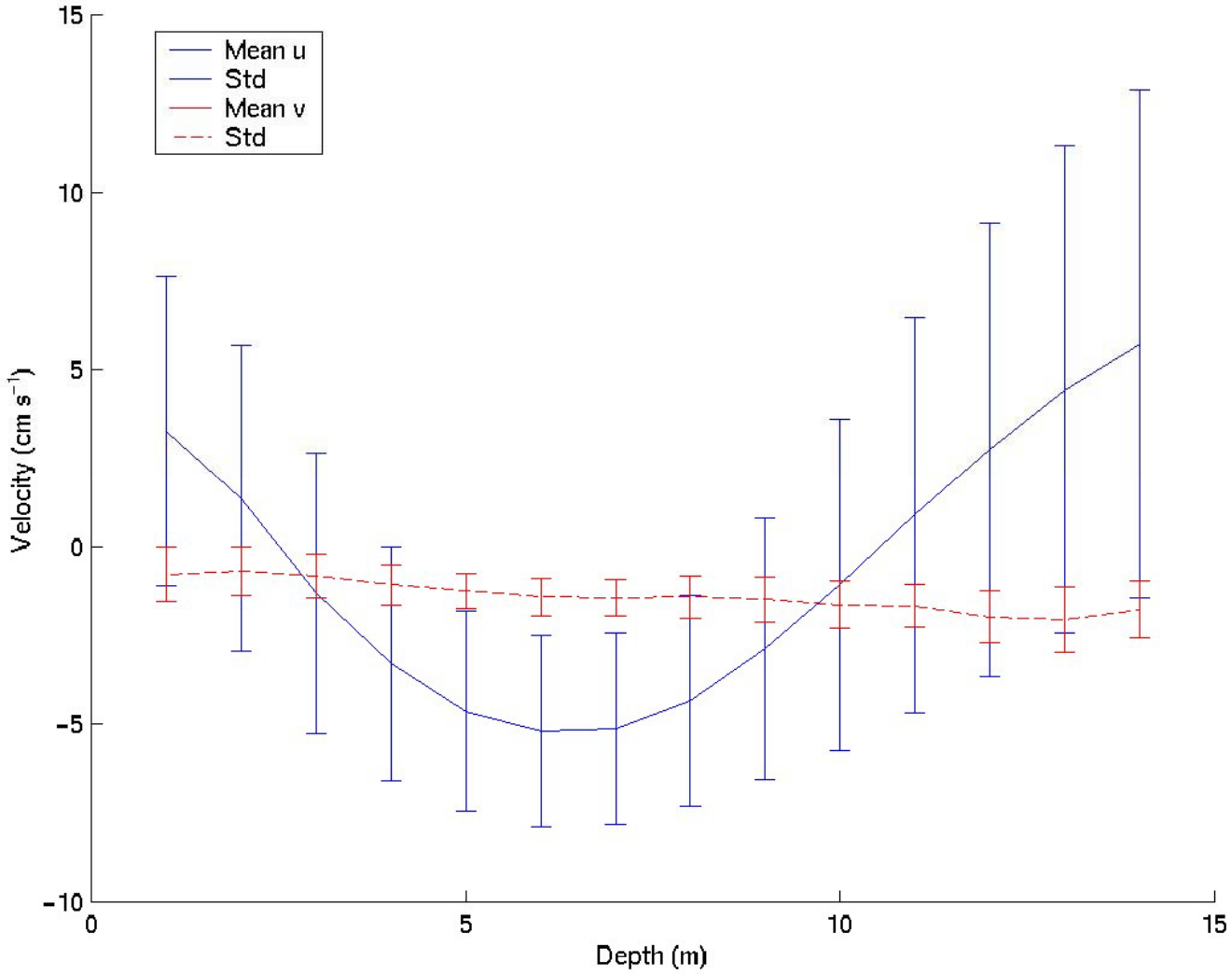

Figure 9: The mean along (solid blue line) and cross (dashed red line) channel velocity profiles. The velocities are in cm s^{-1}. The standard deviation of the velocity components for each depth are plotted as error bars. These velocities are computed in 'channel' co-ordinates (see text).

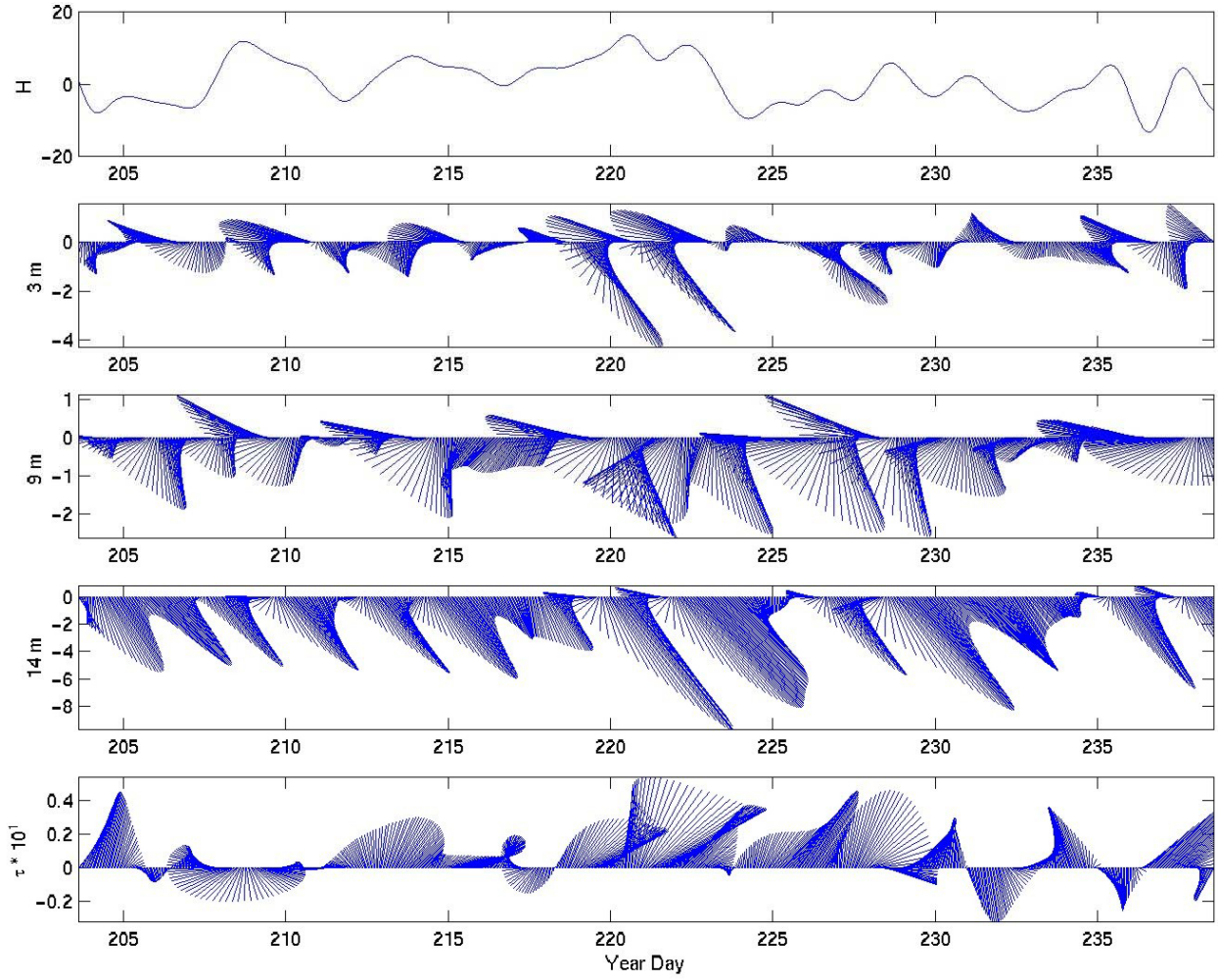

Figure 10: Surface elevation, velocity at 3, 9 and 14 m and wind stress with respect to Earth axes. The horizontal axis doubles as the year day, and the East-West axis, while the vertical axis represents the North-South axis, and shows the scale of the individual physical property. Included here are the surface elevation in cm, the current velocities in cm s^{-1}, and the wind stress in N m^{-2}.

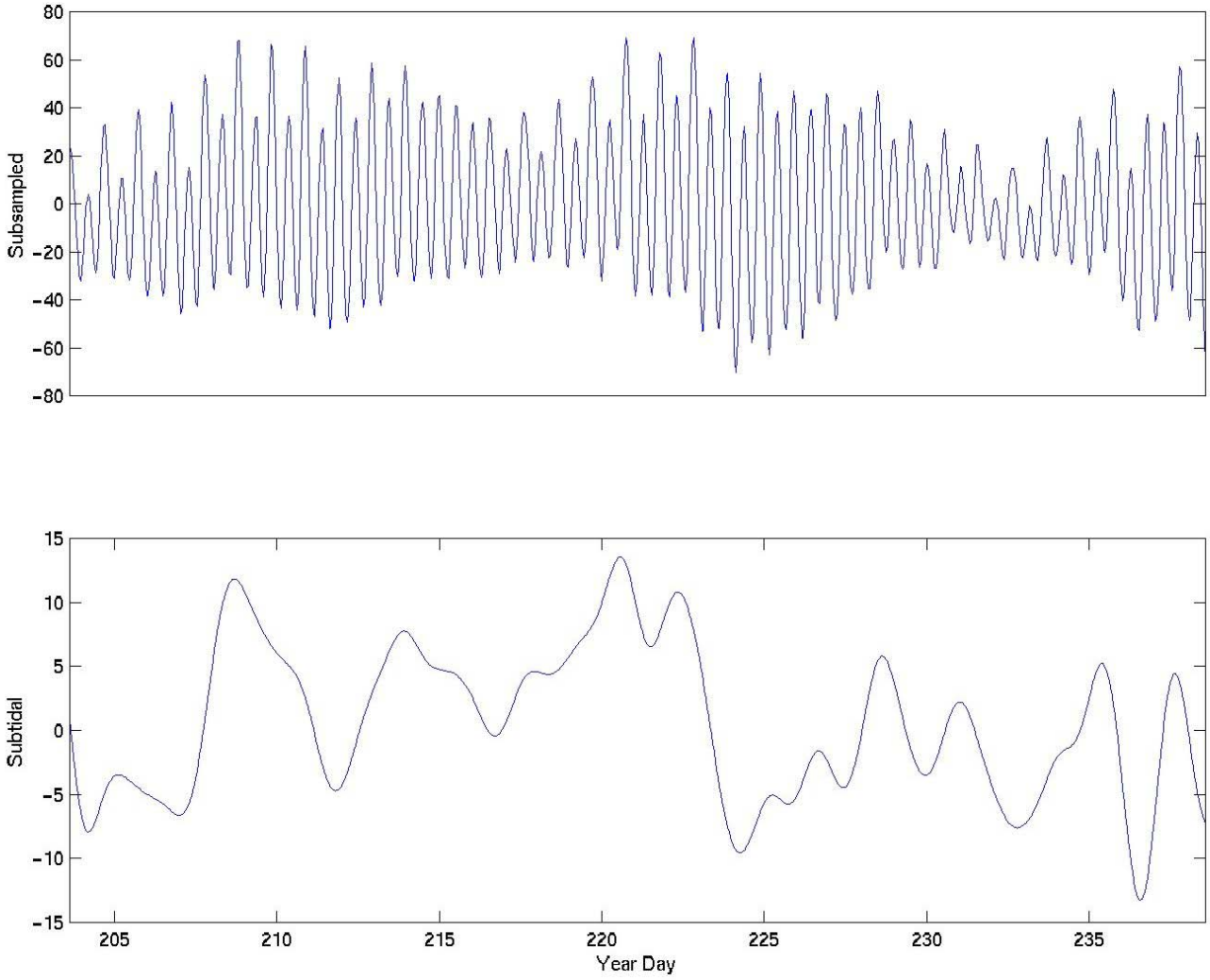

Figure 11: The surface elevation at hourly intervals, and subtidal intervals. In both plots the elevation is measured in cm, and the time line is measured in year day.

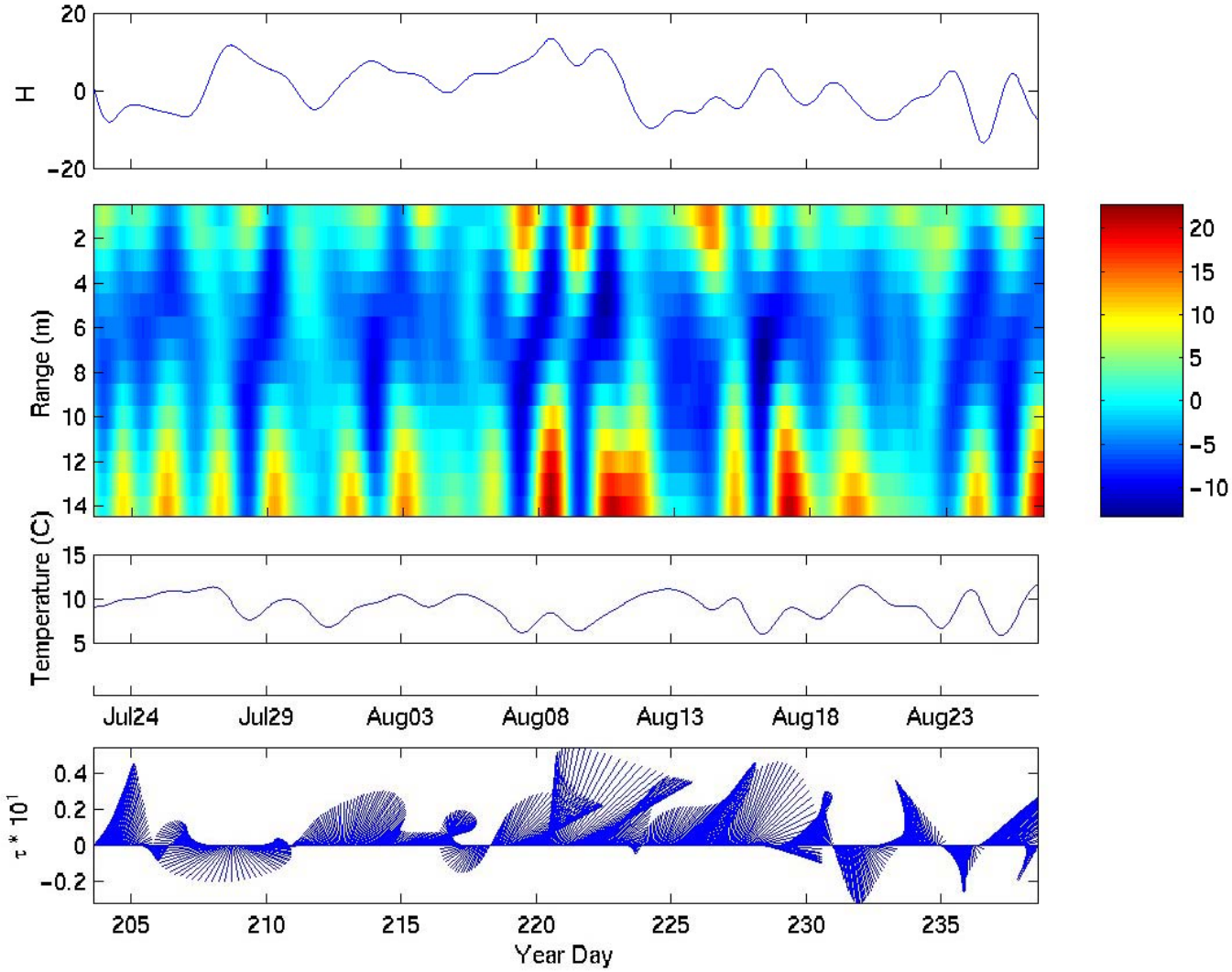

Figure 12: The surface elevation, along channel velocity, temperature and wind stress (with respect to Earth Axes), filtered to remove energy for periods above 1.6 days. The time scale for each plot is in year day, while the individual physical properties are measured in cm, cm s^{-1}, º C, and N m^{-2}.

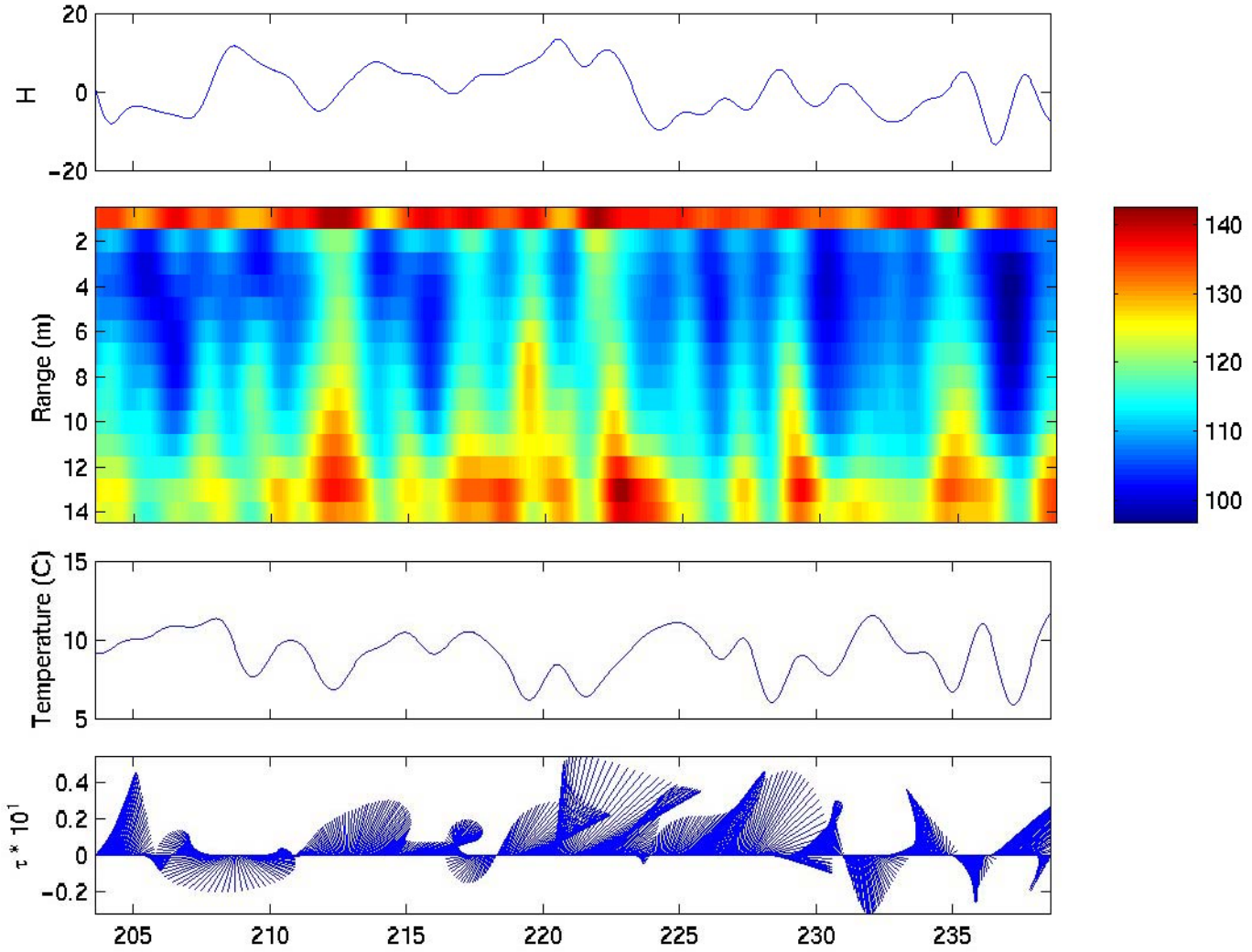

Figure 13: The surface elevation, backscatter intensity, temperature and wind stress, filtered to remove energy for periods above 1.6 days. The time line is in year day, while the individual physical properties are measured in cm, dB, º C, and N m^{-2}.

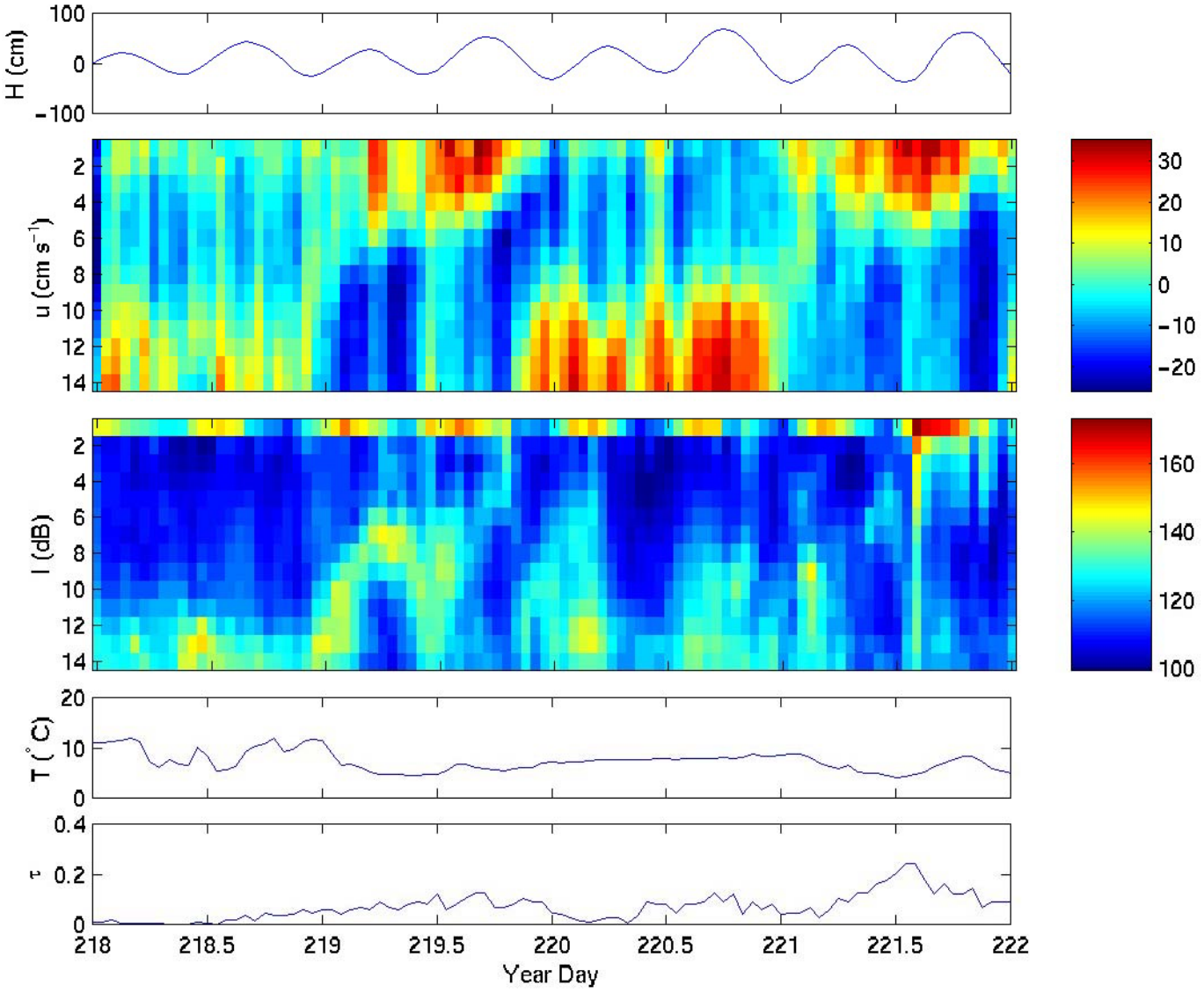

Figure 14: The surface elevation, along channel current velocity, backscatter intensity, temperature and wind stress for Year day 218 to 222. The physical properties are measured in cm, cm s^{-1}, dB, º C, and N m^{-2}.

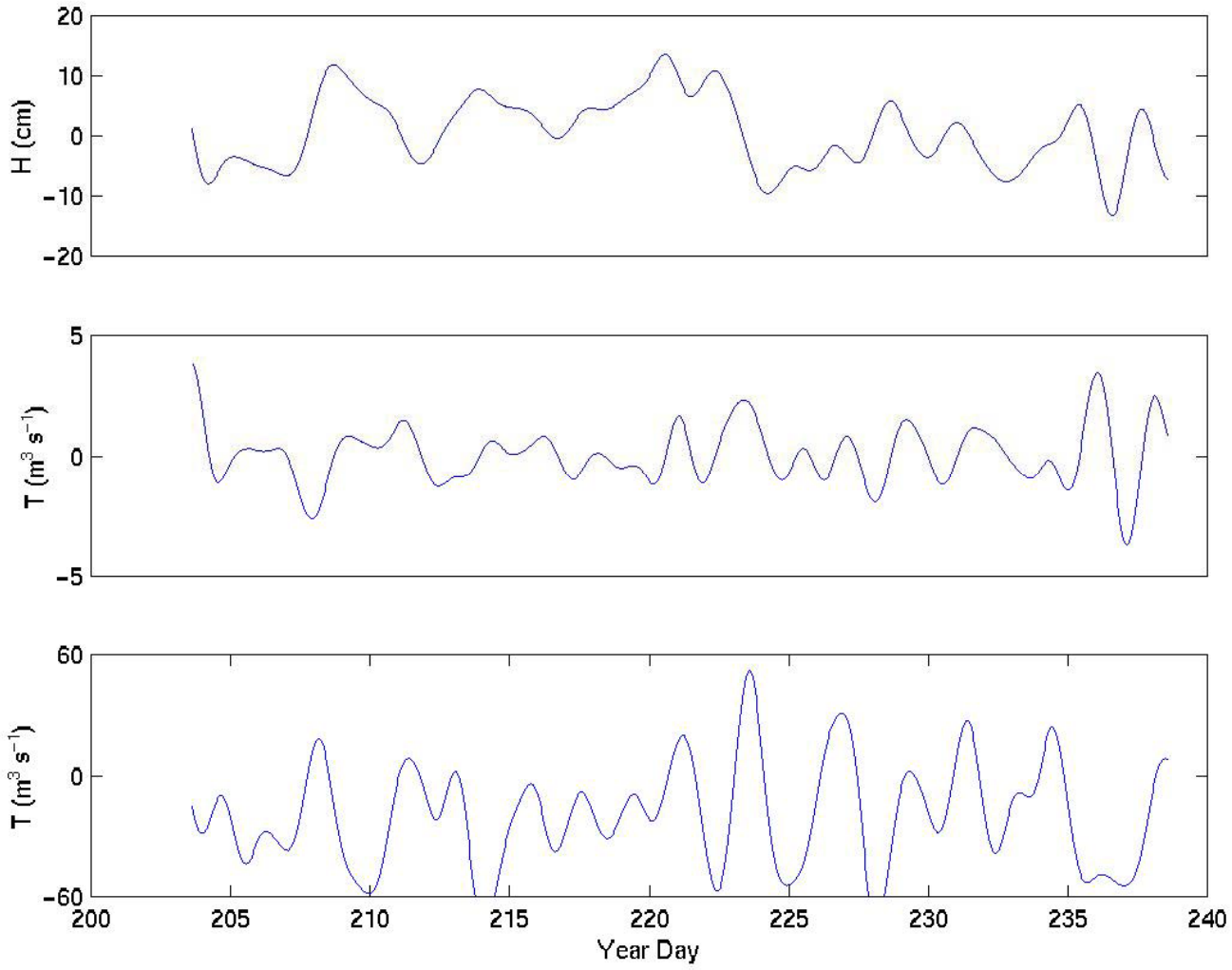

Figure 15: The surface elevation, transport inferred from the measured elevation, and the transport calculated from the along channel velocity component are plotted against year day. The transport is in $m^3\ s^{-1}$, while the surface elevation is in cm.

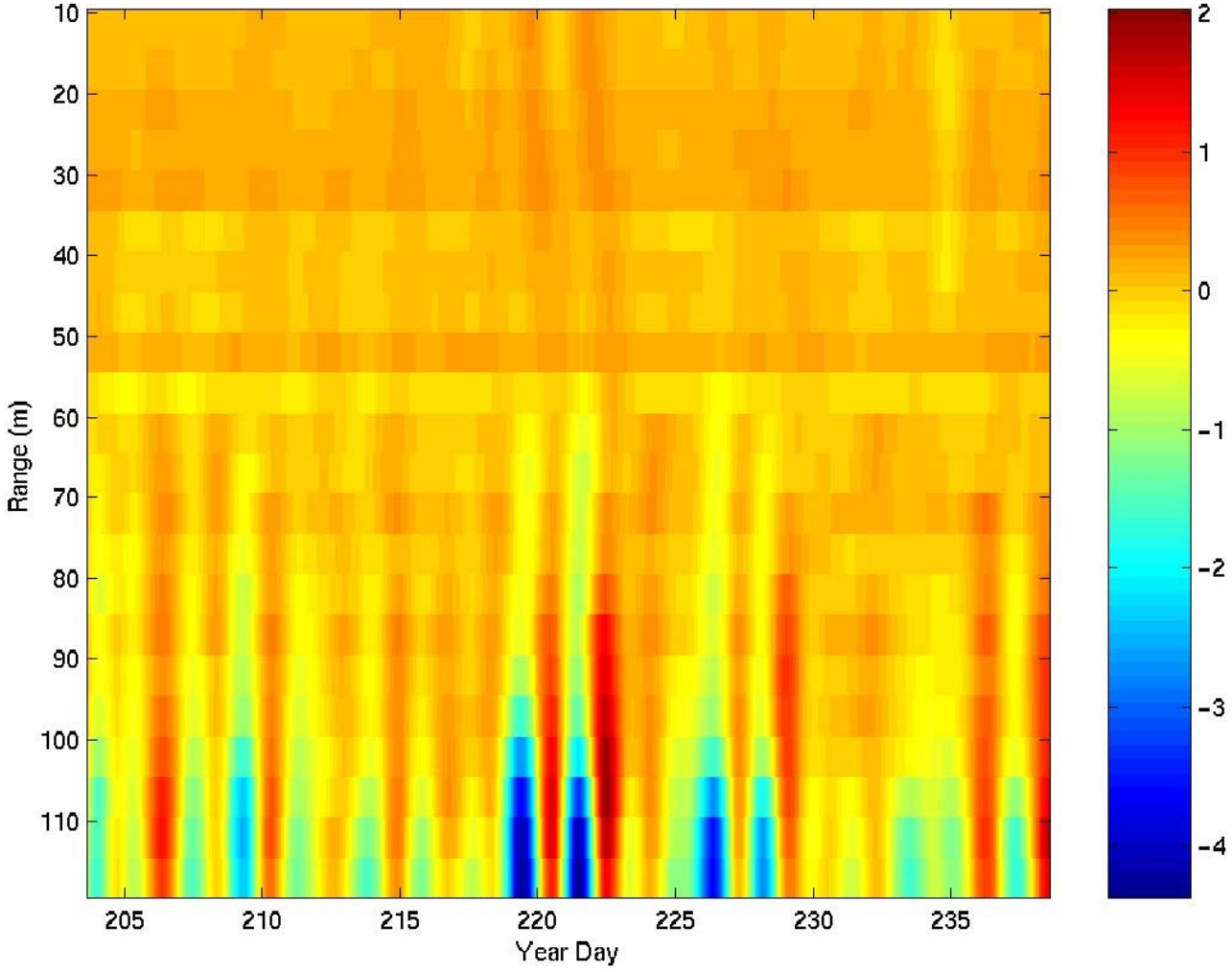

Figure 16: The velocity, in cm s^{-1}, measured by the into-harbour beam of the cross-channel ADCP. The range is the range bin in metres measured from the ADCP. The speed is measured in 'beam' co-ordinates.

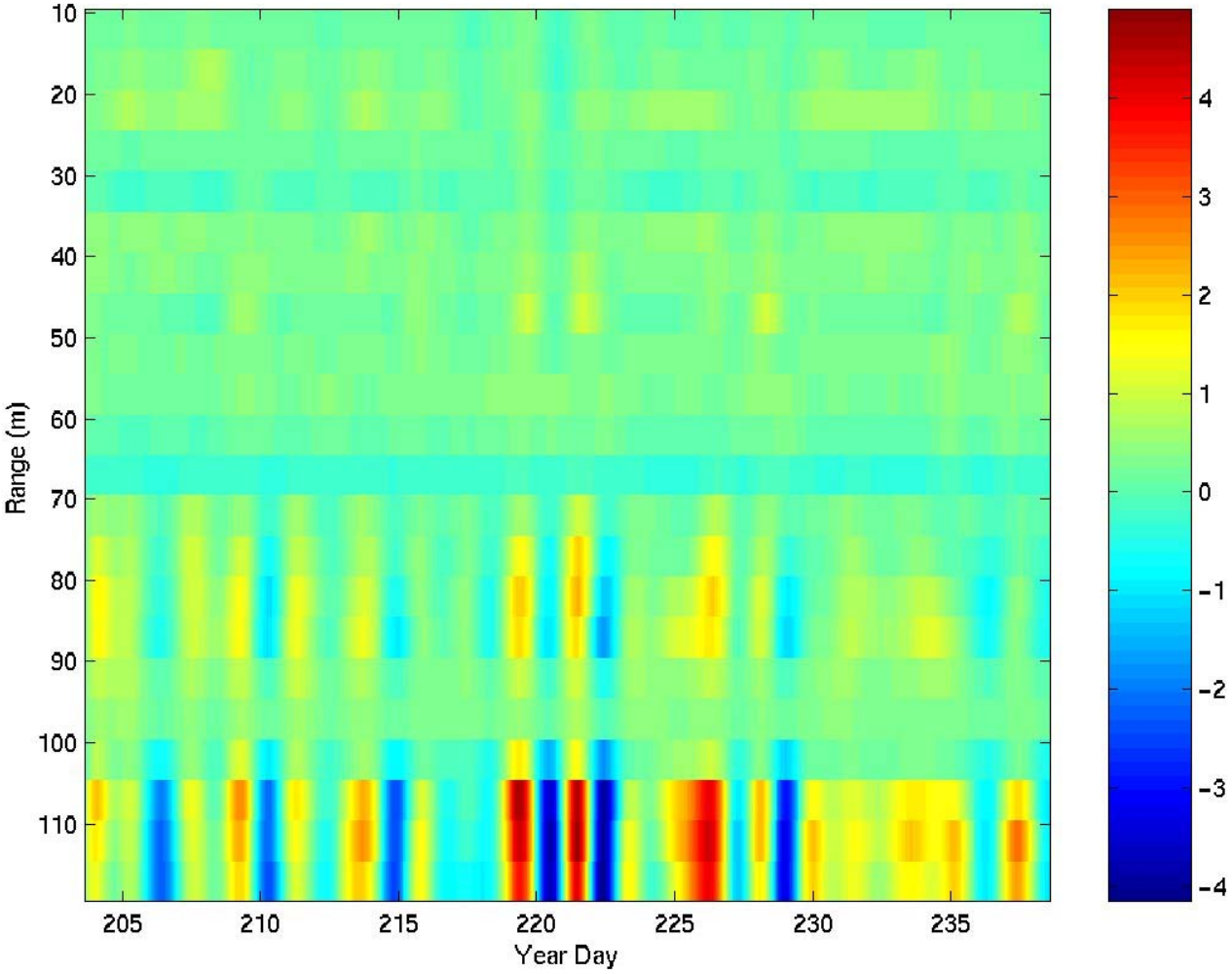

Figure 17: The velocity, in cm s^{-1}, measured by the out-of-harbour beam of the cross-channel ADCP. The range is the range bin in metres measured from the ADCP. The speed is measured in 'beam' co-ordinates.

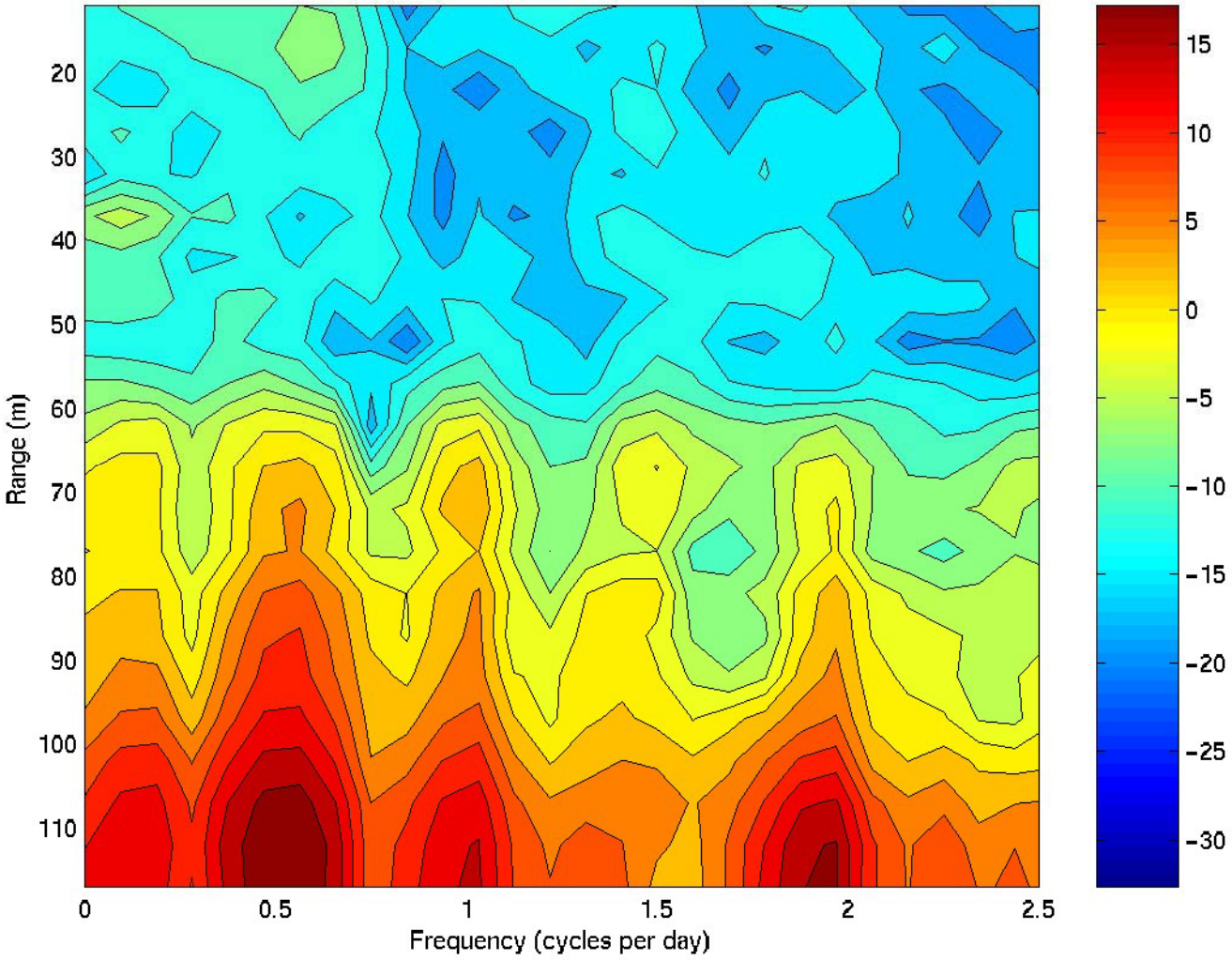

Figure 18: The power spectral density in deciBels for the velocity measured by the into-harbour beam of the cross channel ADCP. The frequency is measured in cycles per day, and the depth is in metres. These spectra have 9 degrees of freedom.

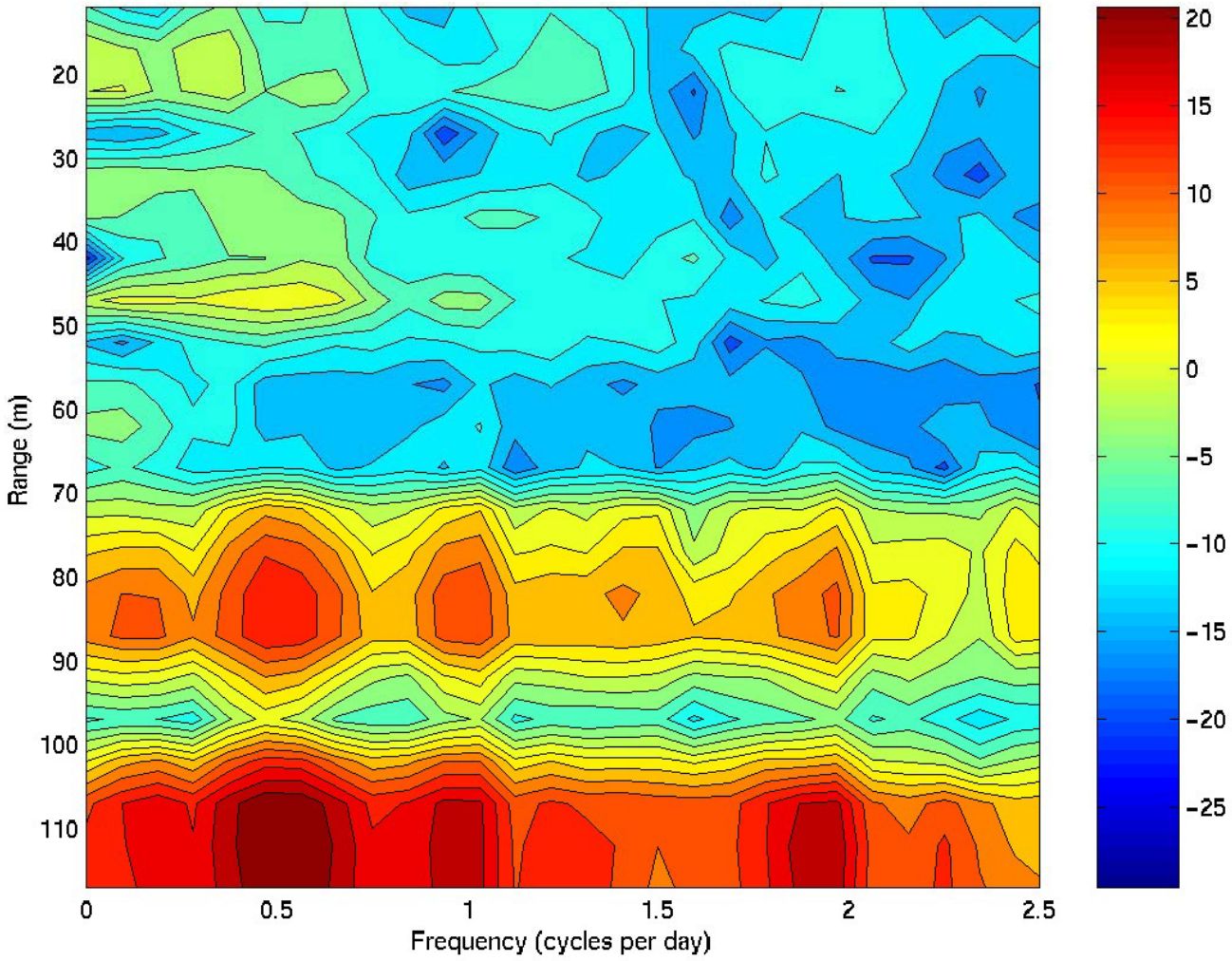

Figure 19: The power spectral density in deciBels for the velocity measured by the out-of-harbour beam of the cross channel ADCP. The frequency is measured in cycles per day, and the depth is in metres. These spectra have 9 degrees of freedom.

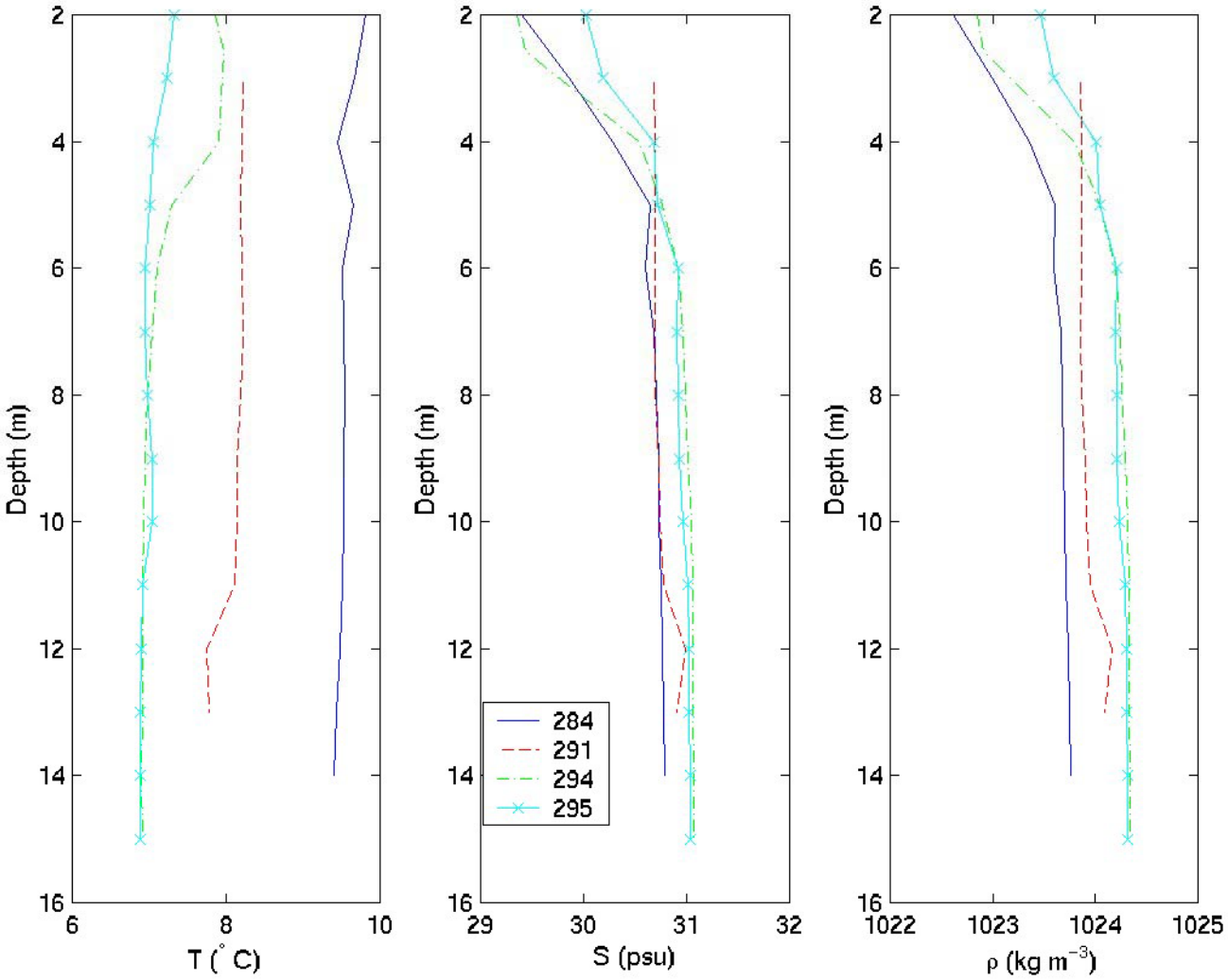

Figure 20: Temperature, salinity, and density profiles for 5 days in October 1999 taken at the mid-channel station.

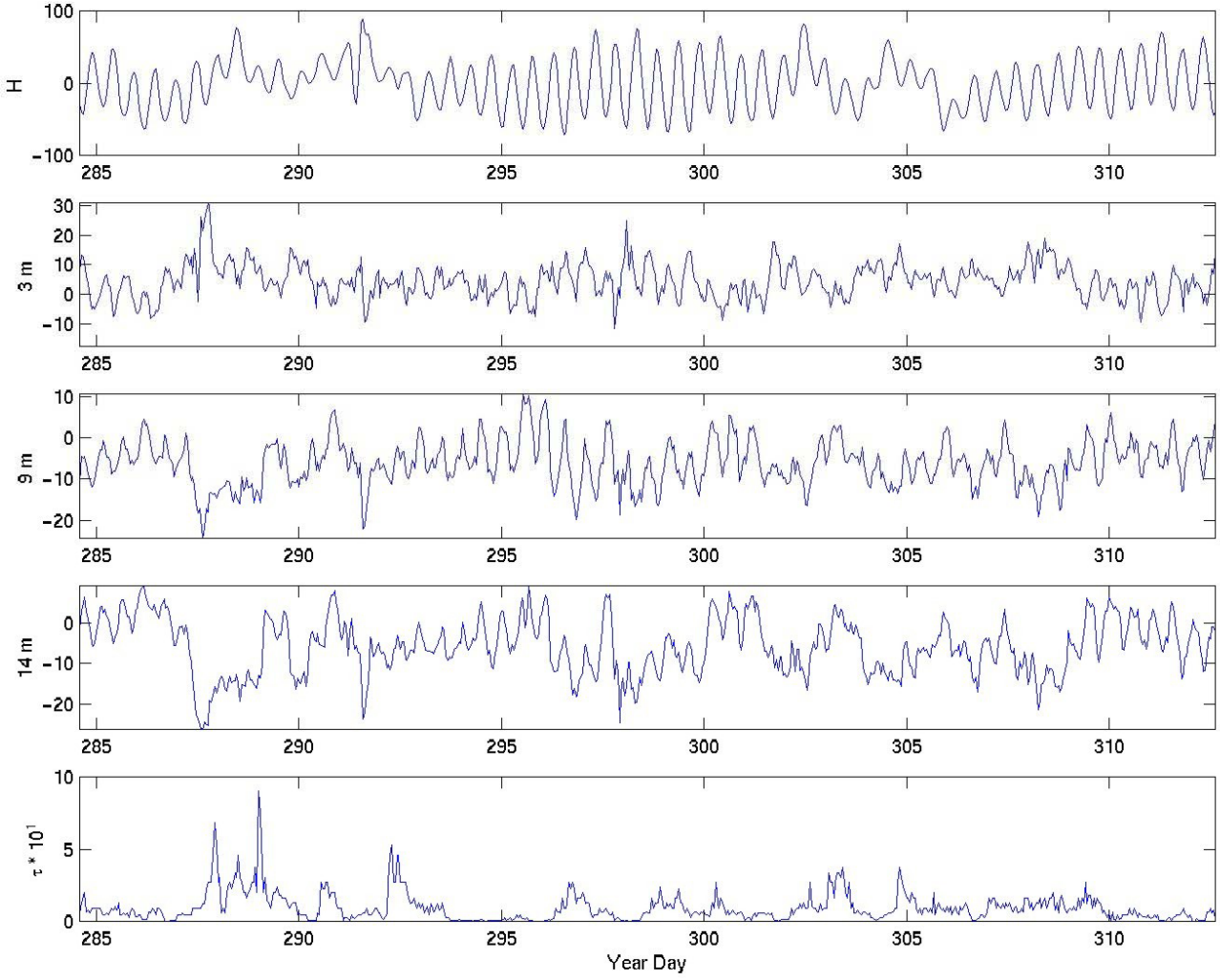

Figure 21: Time series of surface elevation, current velocity along the channel axis (22 degrees from earth axes) at 3, 9 and 14 metres measured at the mid-channel station, and the magnitude of the wind stress. The surface elevation is measured in cm, and the current velocities are in cm s^{-1}. The wind stress amplitude is measured in 0.1 N m^{-2}.

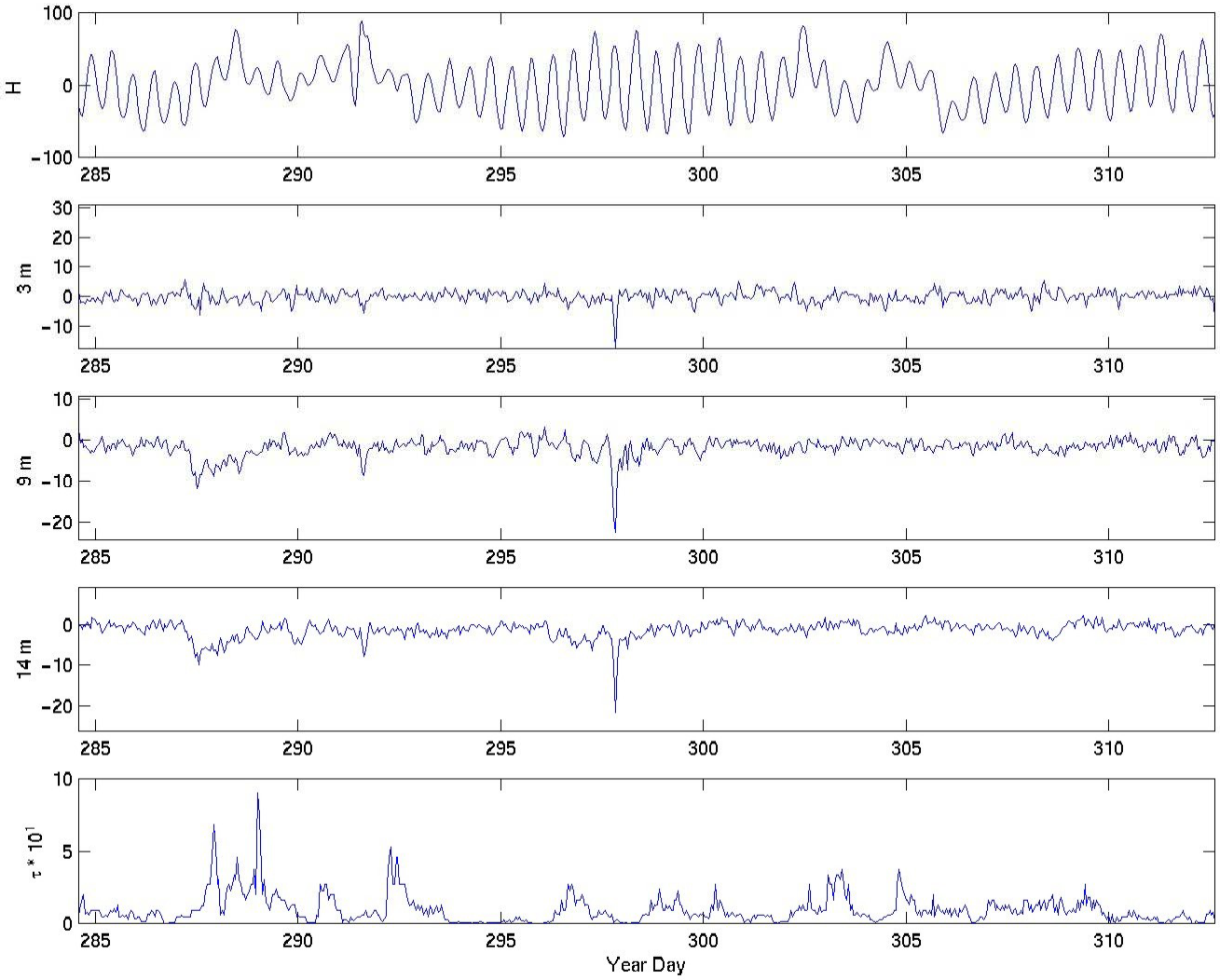

Figure 22: Time series of surface elevation, current velocity across the channel axis (22 degrees from earth axes) at 3, 9 and 14 metres measured at the mid-channel station, and the magnitude of the wind stress. The surface elevation is measured in cm, and the current velocities are in cm s^{-1}. The wind stress amplitude is measured in 0.1 N m^{-2}.

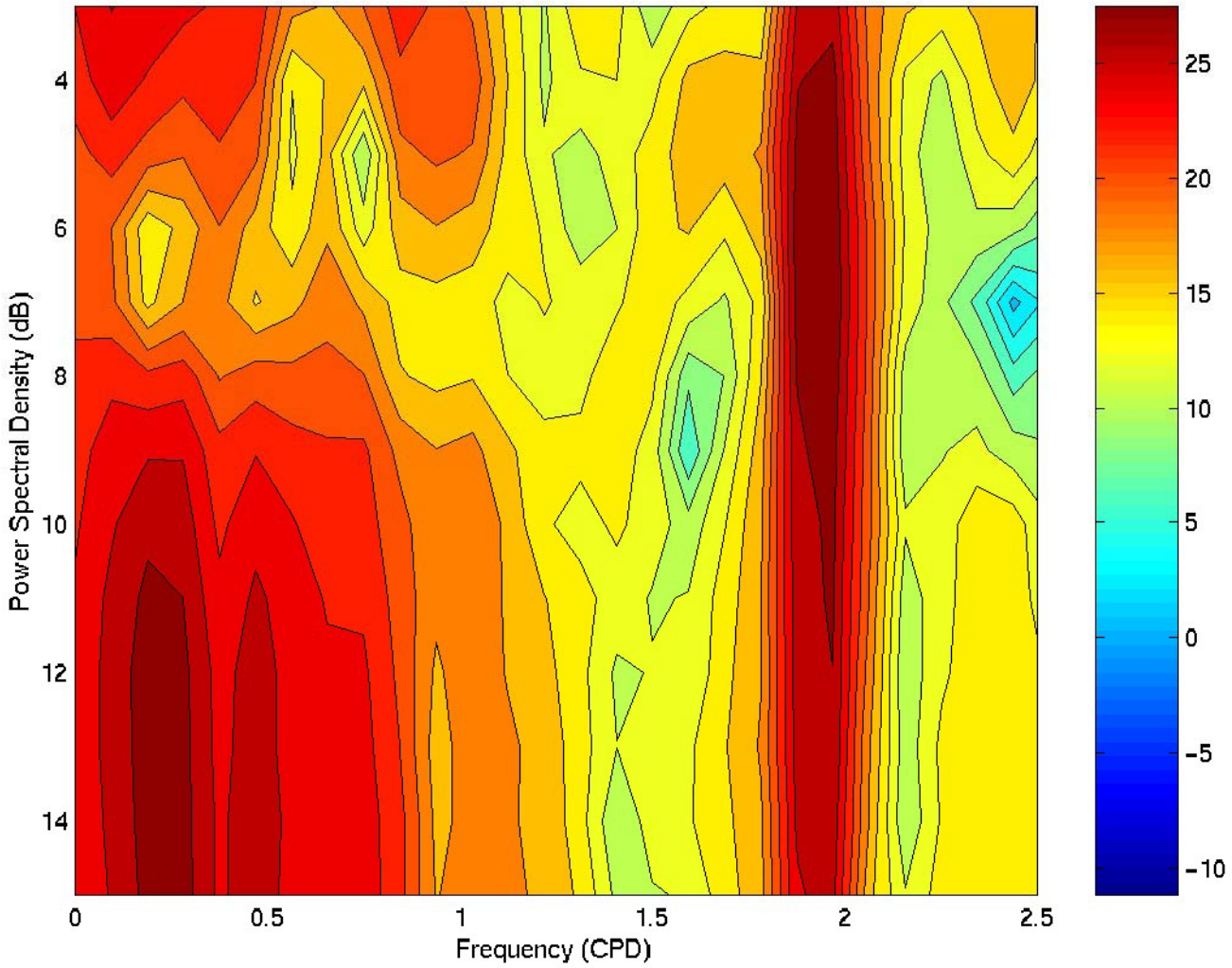

Figure 23: The power spectral density in deciBels for the along channel component of velocity. The frequency is measured in cycles per day, and the depth is in metres. These spectra have 7 degrees of freedom.

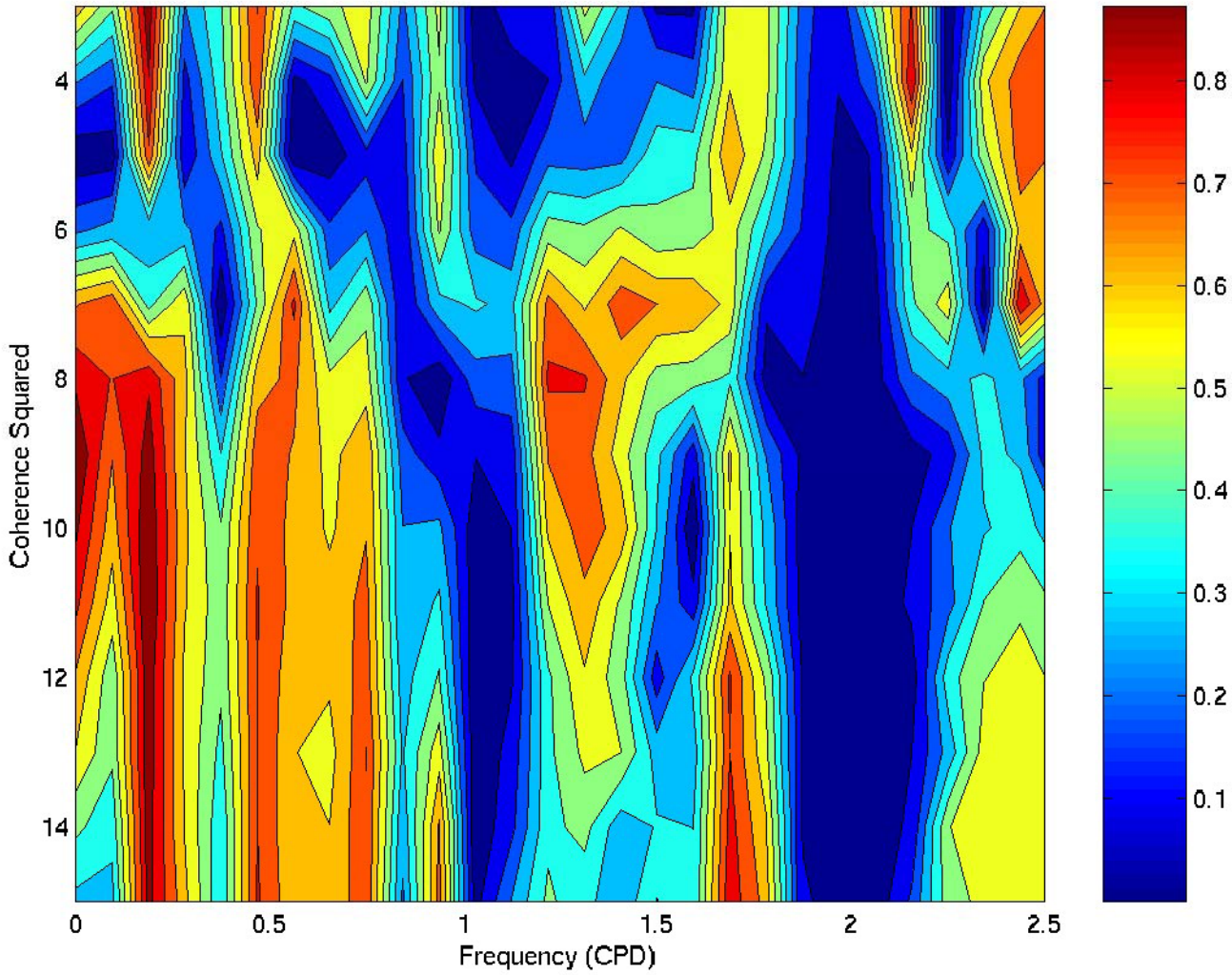

Figure 24: The coherence squared between the East-West component of wind stress and the along channel current velocity. The coherence squared has 7 degrees of freedom.

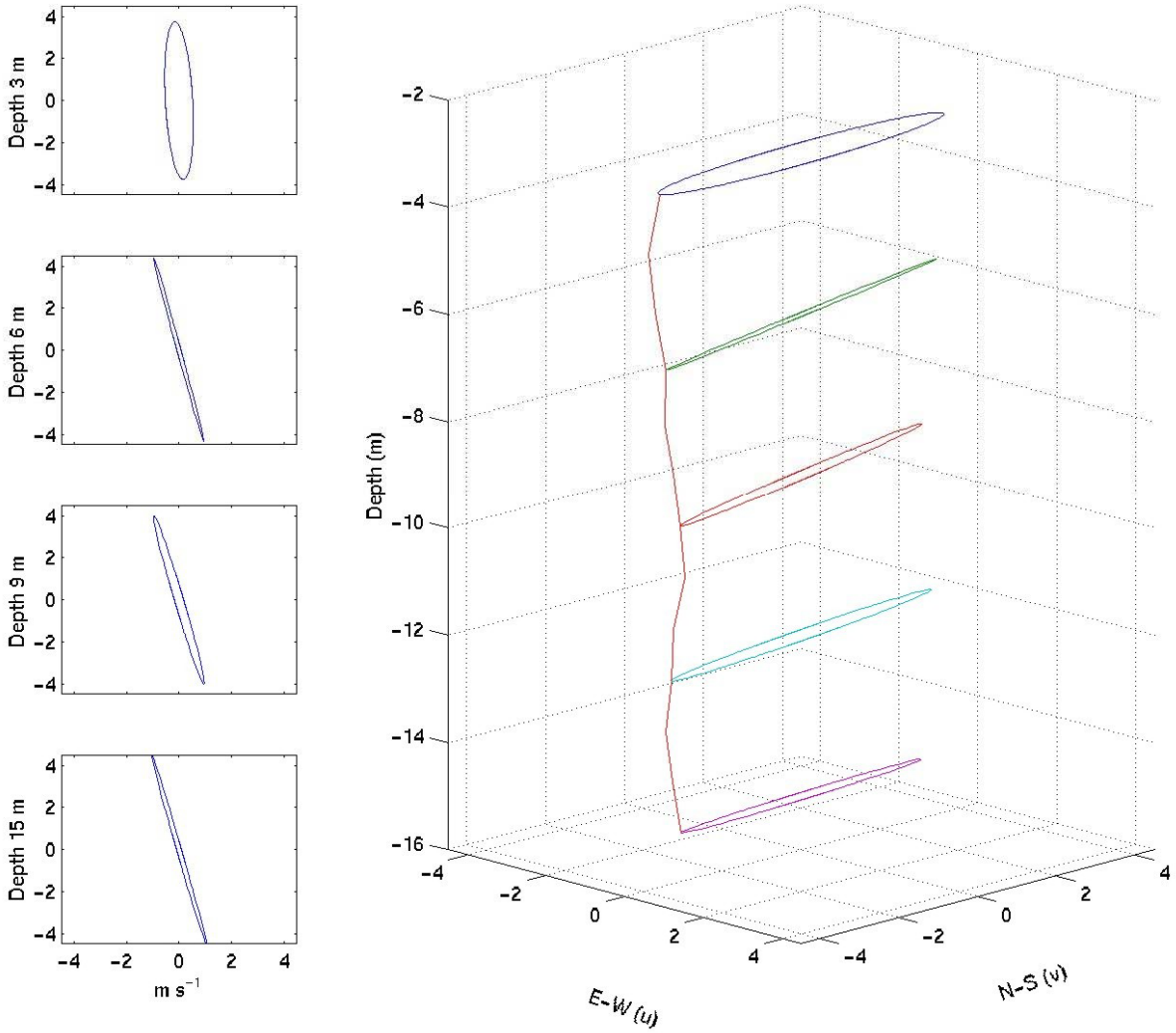

Figure 25: The major and minor axes of the M_2 tidal constituent. The axes represent velocities measured in cm s^{-1}. For the three dimensional plot of the tidal ellipses, the red line represents the inclination of each tidal ellipse at depth, with respect to the rotated axes. Here E-W is the along-channel axis.

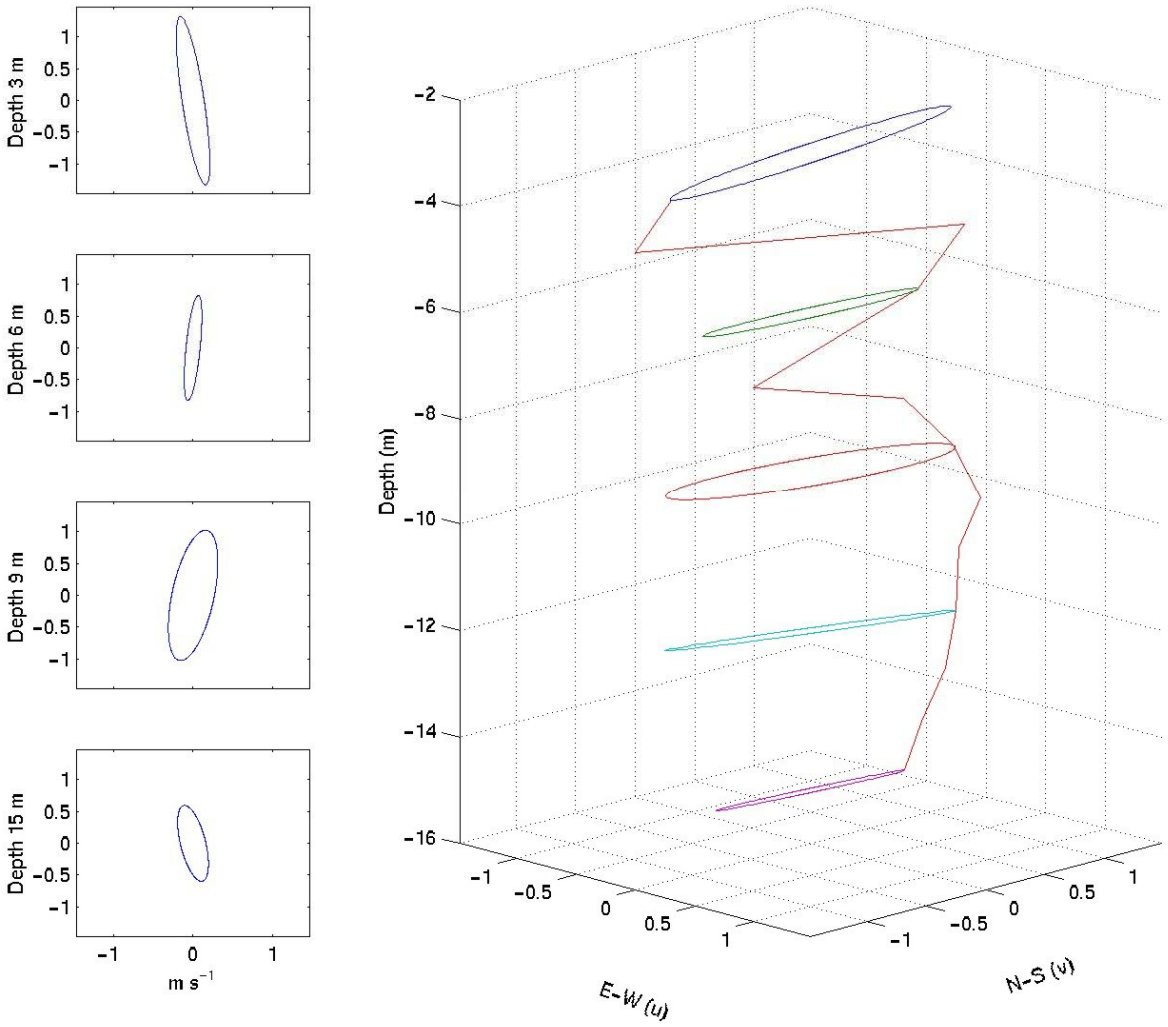

Figure 26: The major and minor axes of the K_1 tidal constituent. The axes represent velocities measured in cm s $^{-1}$. For the three dimensional plot of the tidal ellipses, the red line represents the inclination of each tidal ellipse at depth, with respect to the rotated axes. Here E-W is the along-channel axis.

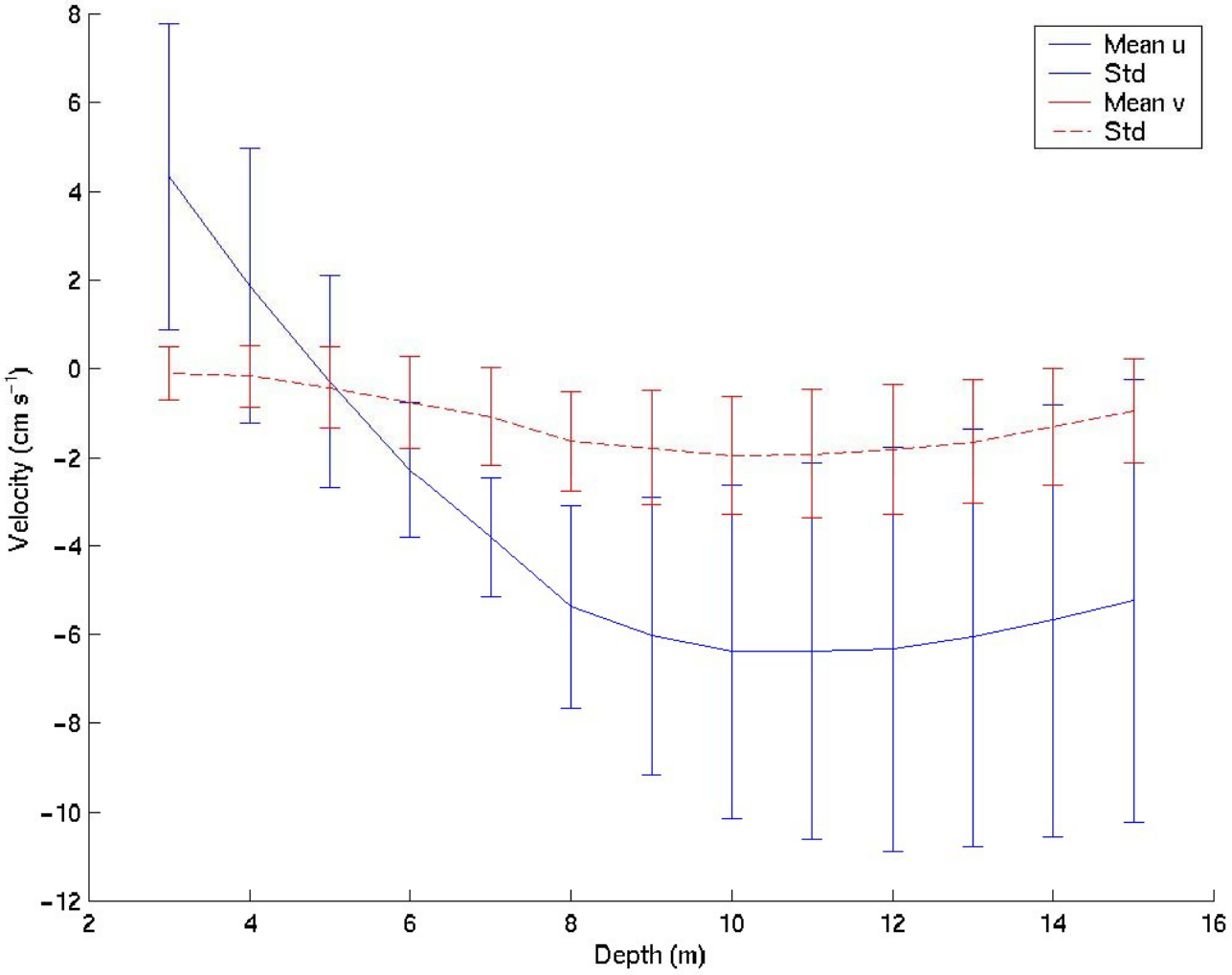

Figure 27: The mean along (solid blue line) and cross (dashed red line) channel velocity profiles. The velocities are in cm s^{-1}. The standard deviation of the velocity components for each depth are plotted as error bars. These velocities are computed in 'channel' co-ordinates (see text).

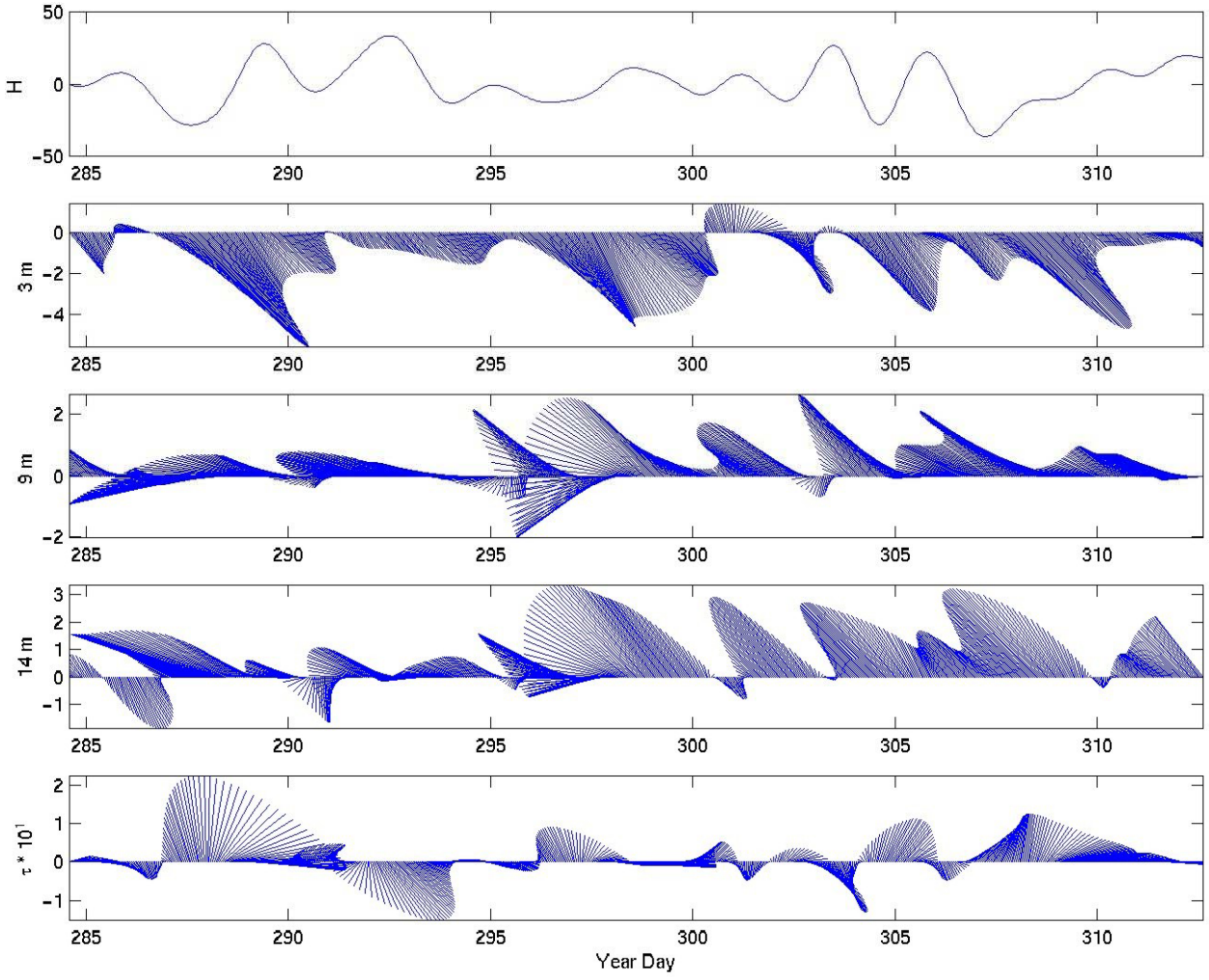

Figure 28: Surface elevation, velocity at 3, 9 and 14 m and wind stress with respect to Earth axes. The horizontal axis doubles as the year day, and the East-West axis, while the vertical axis represents the North-South axis, and shows the scale of the individual physical property. Included here are the surface elevation in cm, the current velocities in cm s^{-1}, and the wind stress in N m^{-2}.

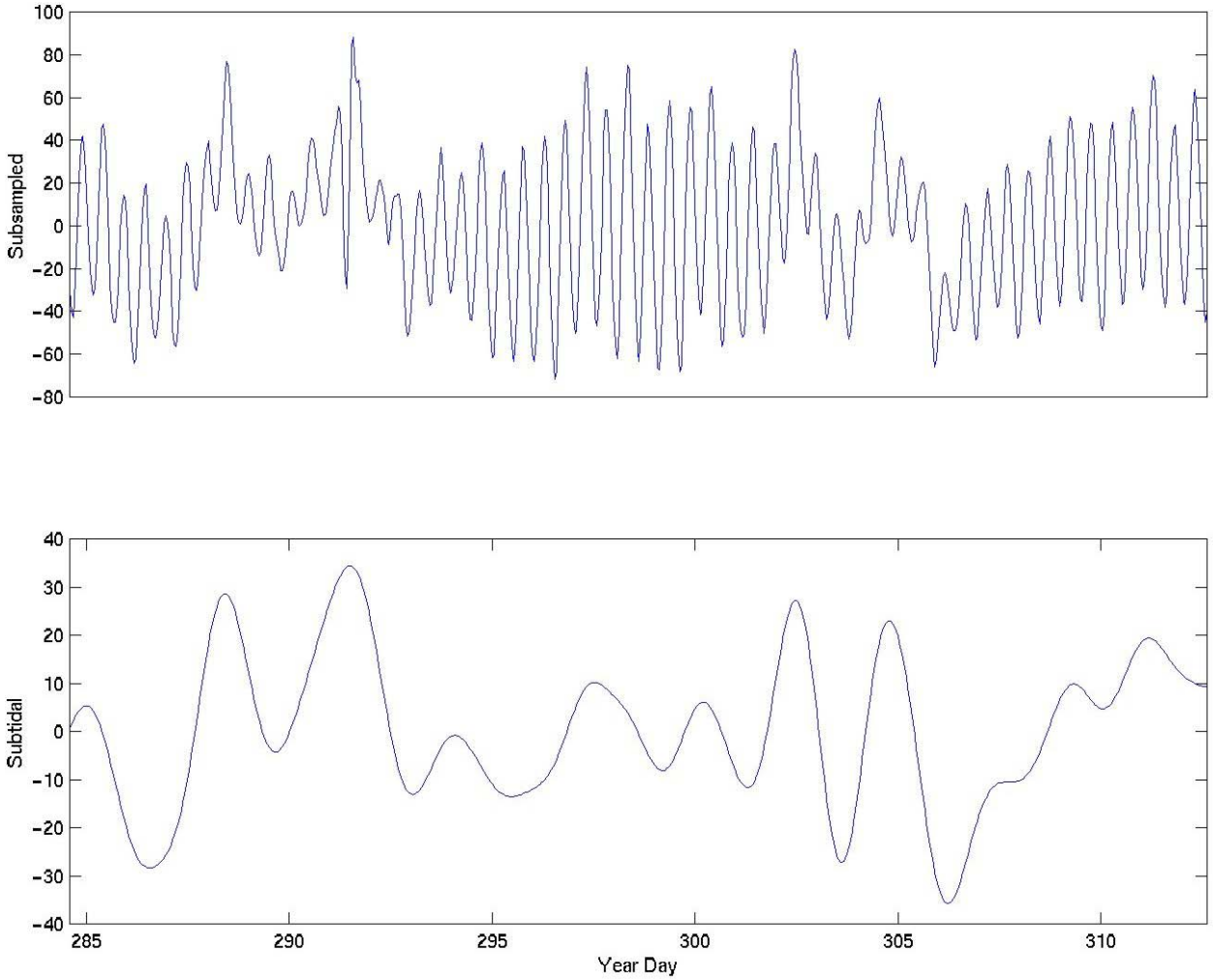

Figure 29: The surface elevation at hourly intervals, and subtidal intervals. In both plots the elevation is measured in cm, and the time line is measured in year day.

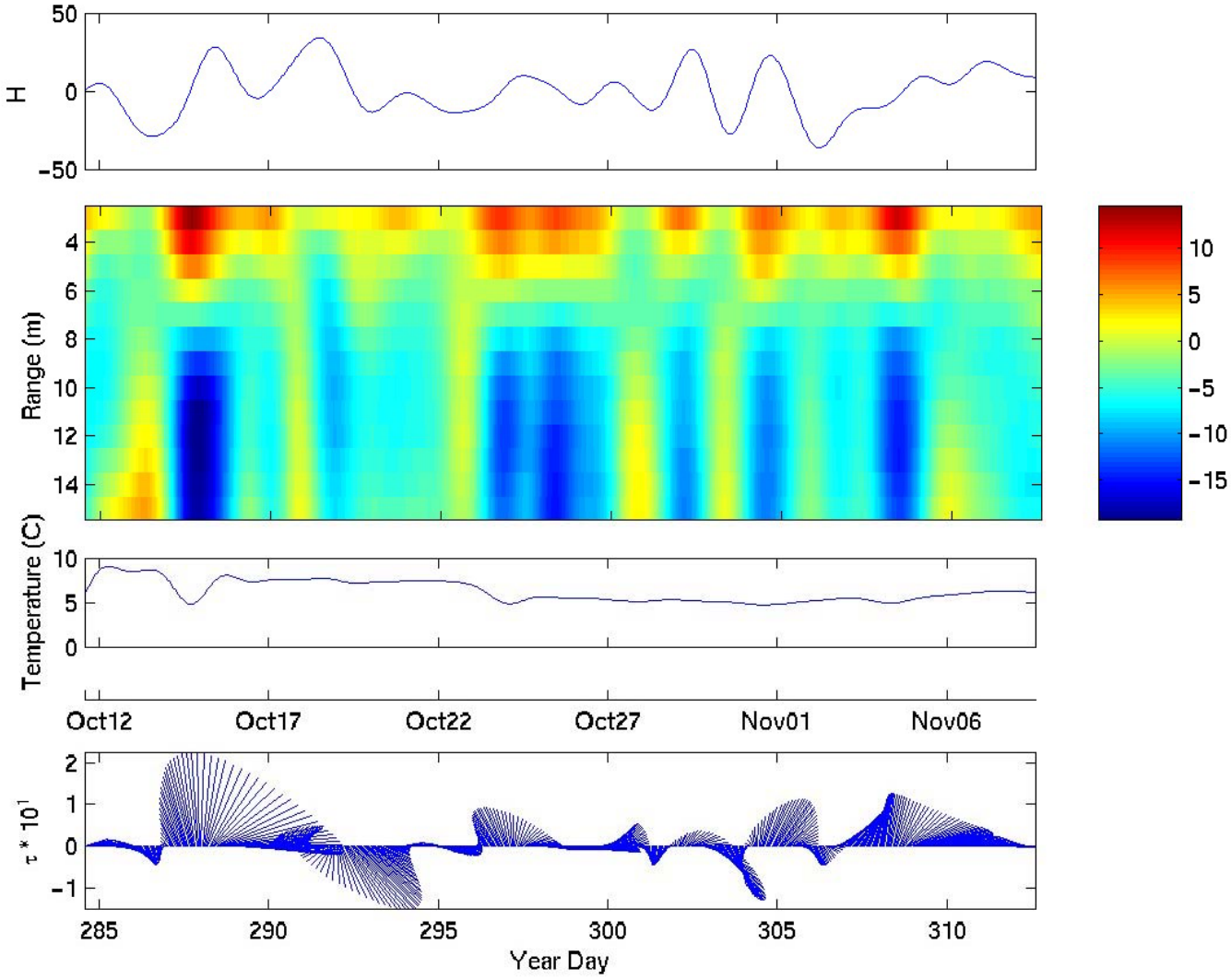

Figure 30: The surface elevation, along channel velocity, florescence, temperature and wind stress (with respect to Earth Axes), filtered to remove energy for periods above 1.6 days. The time scale for each plot is in year day, while the individual physical properties are measured in cm, cm s^{-1}, µ g l^{-1}, º C. and N m^{-2}.

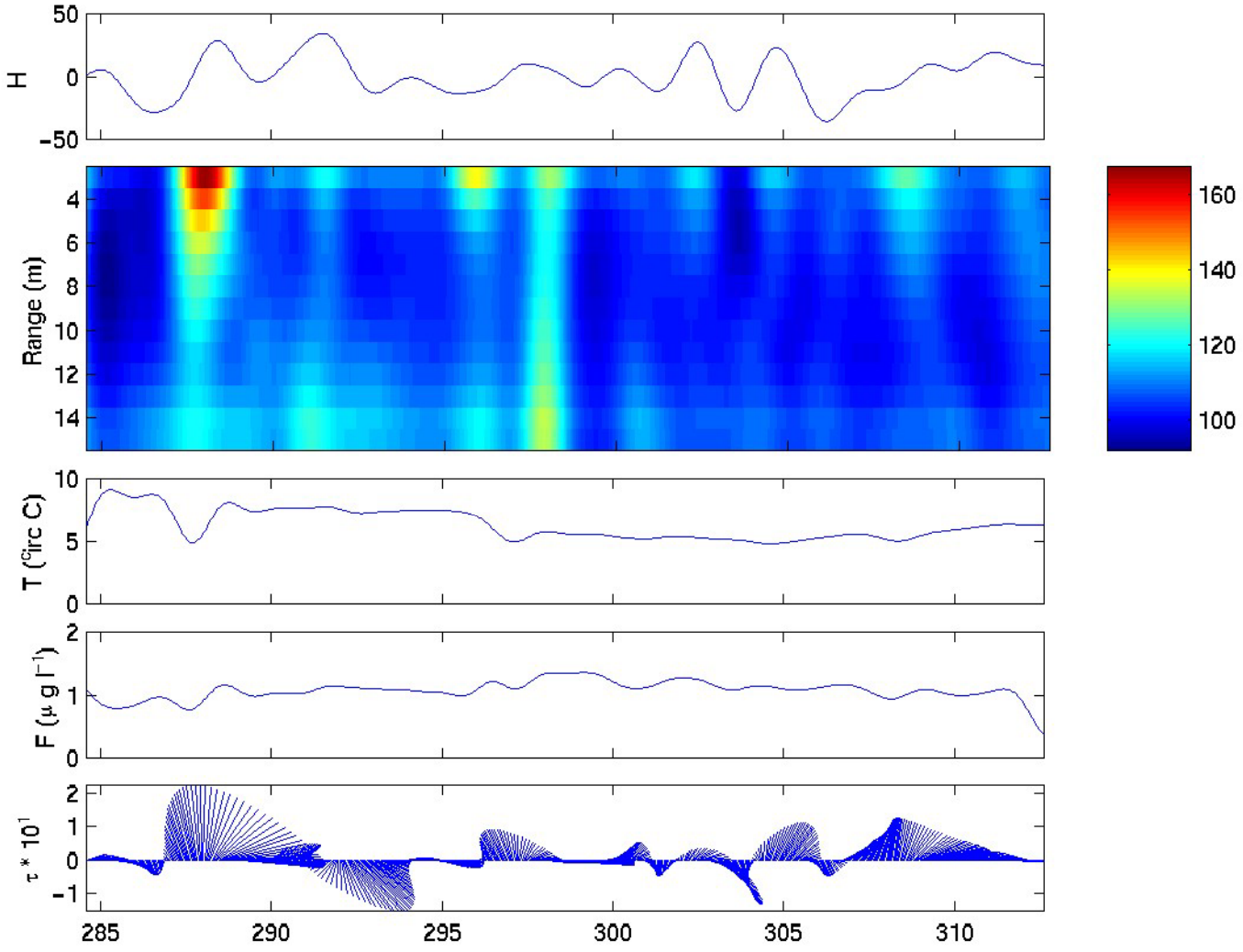

Figure 31: The surface elevation, backscatter intensity, florescence, temperature and wind stress (with respect to Earth Axes), filtered to remove energy for periods above 1.6 days. The time scale for each plot is in year day, while the individual physical properties are measured in cm, cm s^{-1}, μ g l^{-1}, º C. and N m^{-2}.

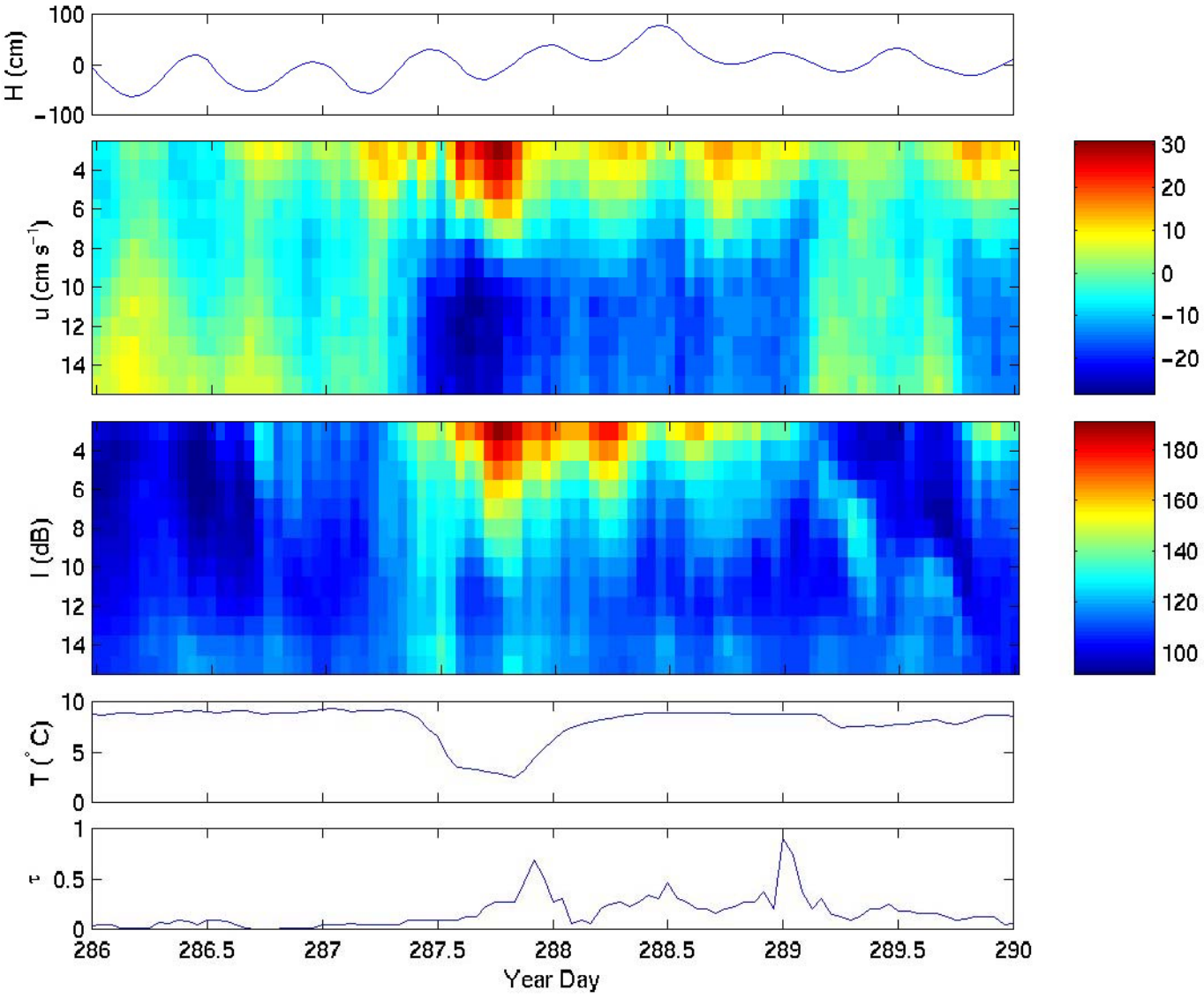

Figure 32: The surface elevation, along channel current velocity, backscatter intensity, temperature and wind stress for Year day 286 to 290. The physical properties are measured in cm, cm s^{-1}, dB, º C, and N m^{-2}.

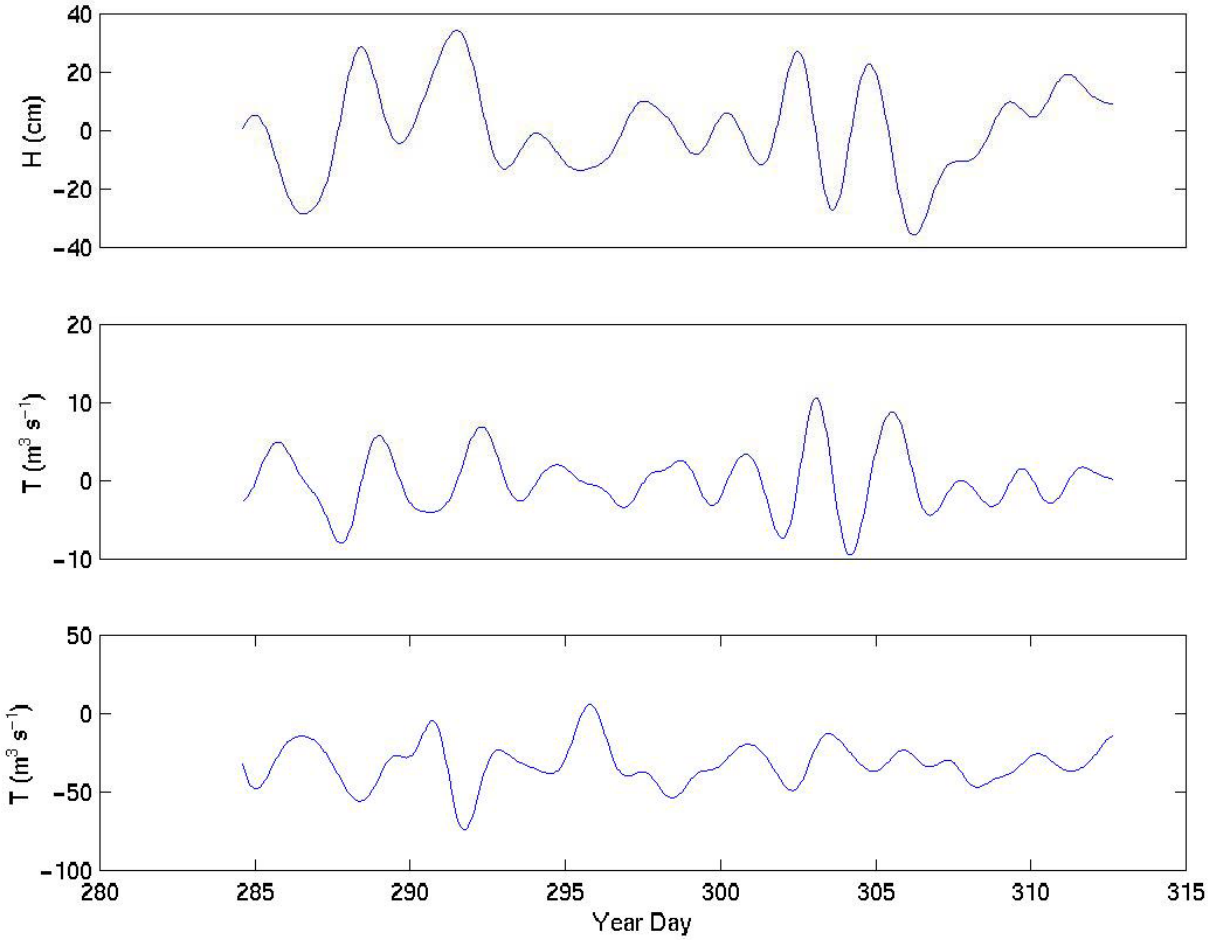

Figure 33: The surface elevation, transport inferred from the measured elevation, and the transport calculated from the along channel velocity component are plotted against year day. The transport is in $m^3\ s^{-1}$, while the surface elevation is in cm.

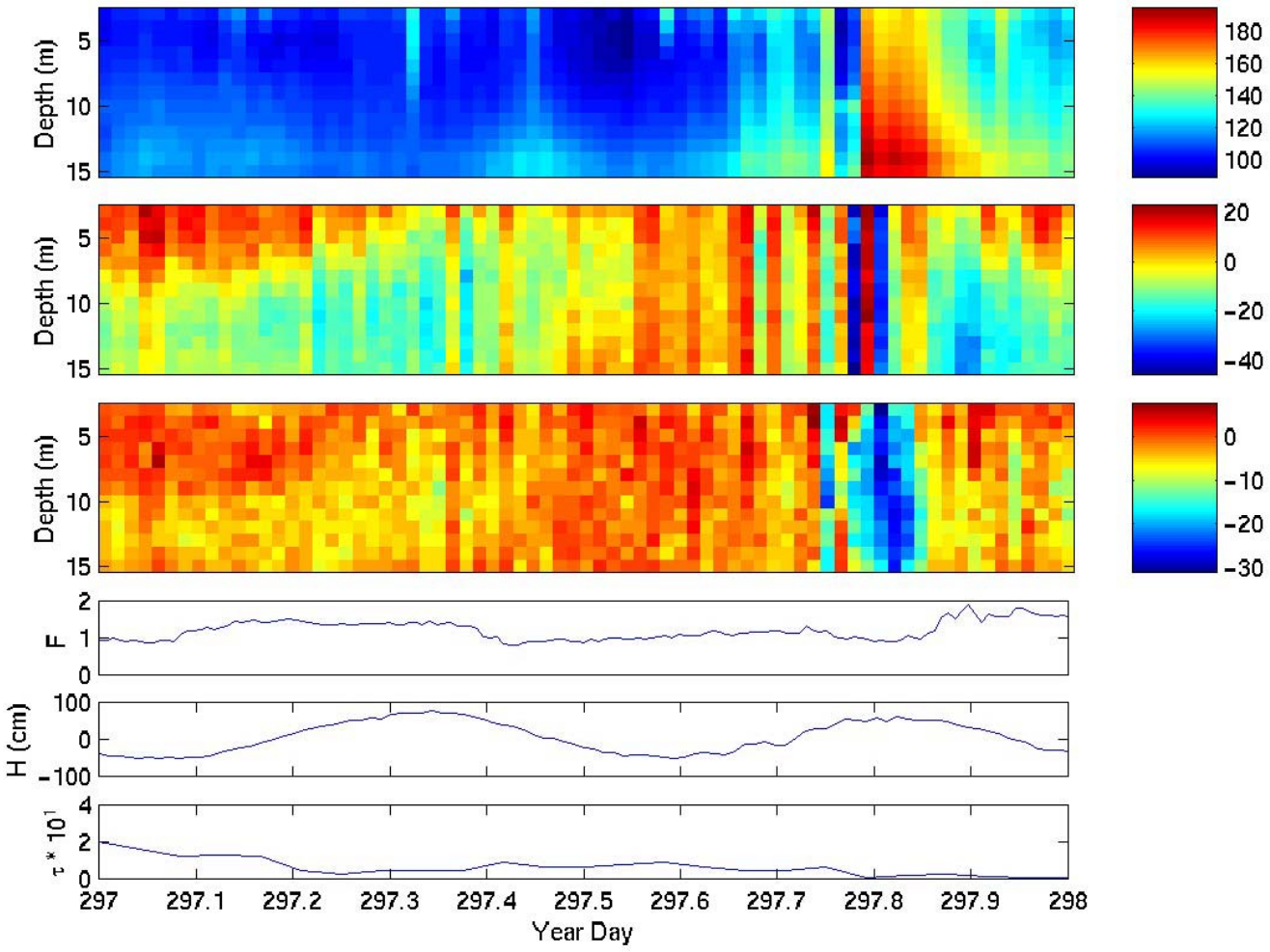

Figure 34: The surface elevation, along channel current velocity, backscatter intensity, florescence, temperature and wind stress (with respect to Earth Axes), filtered to remove energy for periods above 1.6 days. The time scale for each plot is in year day, while the individual physical properties are measured in cm, cm s^{-1}, μ g l^{-1}, º C, and N m^{-2}.